Nucleosynthesis in Neutrino-Driven Winds: I. The Physical Conditions

Y.-Z. Qian

Physics Department, 161-33, California Institute of Technology, Pasadena, CA 91125

and

S. E. Woosley

Board of Studies in Astronomy and Astrophysics, University of California, Santa Cruz,

Santa Cruz, CA 95064

and

Max Planck Institut für Astrophysik, 85740 Garching bei München, Germany

ABSTRACT

During the first 20 seconds of its life, the enormous neutrino luminosity of a neutron star drives appreciable mass loss from its surface. Previous investigations have shown that this neutrino-driven wind could be the site where the r-process occurs. The nucleosynthesis is sensitive to four physical parameters characterizing the wind: its mass loss rate, the entropy per baryon, the electron fraction, and the dynamic time scale. Different authors, using numerical models for supernovae, have arrived at qualitatively different values for these key parameters. Here we derive their values analytically and test our analytic results by numerical calculations using an implicit hydrodynamic code. Employing our analytic and numerical methods, we also investigate how various factors can affect our results. The derived entropy typically falls short, by a factor of two to three, of the value required to produce a strong r-process. Various factors that might give a higher entropy or a more rapid expansion in the wind are discussed.

Subject headings: elementary particles — nuclear reactions, nucleosynthesis, abundances — supernovae: general

1.   Introduction

Recent years have seen progress in our understanding of both the Type II supernova mechanism and heavy element nucleosynthesis. An intriguing suggestion has been that the origin of the r-process is in the neutrino-driven wind of a young neutron star (Woosley & Hoffman 1992, see also Meyer et al. 1992; Howard et al. 1993; Witti, Janka, & Takahashi 1994; and Takahashi, Witti, & Janka 1994). The winds leave the neutron star about 1 to 20 s after its creation by the stellar core collapse. The mass loss is sustained by neutrino heating during the Kelvin-Helmholtz cooling phase of the neutron star. Recently, two groups (Woosley et al. 1994; Takahashi et al. 1994) have published calculations of r-process in these neutrino-heated ejecta based upon different supernova models. These calculations yield tantalizing results compared with the observed solar system abundance distribution of r-process elements, but the calculations share some drawbacks and exhibit differences.

One failure common to all calculations so far is the overproduction of nuclei in the vicinity of the magic neutron shell, $N = 50$, specifically ^{88}Sr, ^{89}Y, and ^{90}Zr. Interestingly, this difficulty can be circumvented and even used to provide some attractive nucleosynthesis of the light p-process nuclei if the electron fraction Y_e in the ejecta is increased slightly from the value found by Wilson in Woosley et al. (1994). Hoffman et al. (1996a) have shown that for $0.484 \lesssim Y_e \lesssim 0.488$, the problematic nucleosynthesis disappears. This result highlights the need for a detailed and accurate analysis of Y_e obtained in the wind, and also hints at some critical uncertainties in the supernova models.

A second difficulty is that various calculations do not agree on the entropy in the wind at the time the r-process is alleged to occur. Woosley et al. (1994) based their calculations on a supernova model computed by Jim Wilson, where high entropies, $\sim 400 \, k$ per baryon (hereafter, we frequently refer to entropy without its units in Boltzmann constant k per baryon), were obtained at times later than about 10 seconds. These high entropies were very

beneficial, perhaps even necessary for the production of nuclei with mass number $A \gtrsim 130$ and especially the r-process abundance peak at $A \sim 195$. However, in the supernova model evolved by Janka and employed in the calculations of Witti et al. (1994) and Takahashi et al. (1994), entropies of only $\lesssim 100$ were obtained. In fact, Takahashi et al. (1994) had to artificially impose an increase by a factor of ~ 5 in the entropy to obtain a successful r-process. Similar small values of the entropy were also obtained in numerical calculations by Woosley (1993 and unpublished). This difference further demonstrates the necessity of an unambiguous understanding of the physical conditions obtained in the neutrino-driven wind.

Finally, Meyer (1995) has recently shown that the r-process in the neutrino-heated supernova ejecta might be seriously affected by neutrino spallation reactions on α-particles under conditions obtained in Wilson's supernova model. These reactions were neglected in the previous r-process calculations. Inclusion of these reactions reduces the production of nuclei with $A \sim 195$ in Wilson's supernova model. To counter the damaging effects of neutrino spallation reactions on α-particles requires an entropy even higher than ~ 400, a lower electron fraction, a shorter dynamic time scale, a larger distance of the r-process site from the neutrino source, or some combination of the above.

It is clear then that a careful analysis of the physical conditions in the neutrino-driven wind is needed. These conditions include the entropy per baryon, the electron fraction, the dynamic time scale, and the mass outflow rate. While simple analytic calculations cannot give the full detail of a multidimensional numerical study with non-LTE treatments of neutrino transport, they can be very useful for understanding the output from the numerical codes and delimiting, from first principles, likely ranges for the conditions. That is the chief goal of this paper.

Because the conditions relevant for heavy element nucleosynthesis exist, in terms of

neutron star time scales, long after the shock has been launched in a successful supernova explosion, the neutrino-driven wind can be reasonably approximated as a quasi-steady spherical outflow. This assumption is borne out by the recent two-dimensional numerical calculations by Janka and Müller (1995). This fact facilitates analytic studies of the neutrino-driven wind, and greatly simplifies the numerical treatment (though we shall also briefly examine non-steady outflow). It also has the consequence that our key results are independent of the details of how the shock gets launched.

In §2, we set up the basic equations for analytic studies of the neutrino-driven wind. Our work here is similar in ways to that of Duncan, Shapiro, and Wasserman (1986), but more extensive and directed towards nucleosynthetic issues. The relevant initial and boundary conditions and the input neutrino physics to solve these equations are discussed, and we present the analytic results for the entropy per baryon, the dynamic time scale, and the mass outflow rate in the ejecta in §3. In §4, we compare these analytic results with numerical calculations using an implicit hydrodynamic code KEPLER while varying the neutron star mass, radius, and neutrino luminosity. Some dependencies upon the Newtonian approximation, the steady-state assumption, boundary pressure, and additional energy sources are also briefly explored. In §5, we discuss how the electron fraction Y_e is determined in the ejecta, and present a novel neutrino "two-color plot" that aids in understanding, qualitatively, the nature of heavy element nucleosynthesis in supernovae. In §6, we discuss the dependence of a successful r-process on the set of three physical parameters: the entropy per baryon, the electron fraction, and the dynamic time scale, and speculate further on how various factors can affect the properties of the neutrino-driven wind. In a separate paper (Hoffman et al. 1996b), we will give a detailed discussion of the implications of our results for heavy element nucleosynthesis in supernovae.

2. Equations to model the neutrino-driven wind

The time of interest here is later than about 1 s after the shock has been launched in a successful Type II or Ib supernova. By this time the shock wave responsible for the supernova explosion has reached a radius of about 10 thousand kilometers and the temperature at that shock has declined to about a billion degrees. A hot neutron star with a radius of ~ 10 km lies near the center of this supernova. Its Kelvin-Helmholtz phase of cooling by neutrino emission lasts about 10 s, during which time the gravitational binding energy of the final neutron star, a few times 10^{53} erg, is radiated approximately equally in ν_e, $\bar{\nu}_e$, ν_μ, $\bar{\nu}_\mu$, ν_τ, and $\bar{\nu}_\tau$ (Janka 1995). Therefore, the average luminosity for a specific neutrino species at this late time is of order 10^{51}–10^{52} erg s^{-1}. As this neutrino flux streams through the region above the neutron star, the following weak interactions can take place: absorption of ν_e and $\bar{\nu}_e$, neutrino-electron scattering, and neutrino-antineutrino annihilation. The last two are experienced by all flavors of neutrinos. These interactions transfer energy from neutrinos to the matter above the neutron star and heat it. Consequently, this material expands away from the neutron star and develops into a mass outflow we call the "neutrino-driven wind."

Intuitively, once the convection associated with the launching of the shock has ceased, one expects this mass outflow to be relatively smooth, and adequately described by a quasi-steady-state approximation. In fact, this expectation is verified by recent two-dimensional numerical simulations (Janka and Müller 1995). This is because during the Kelvin-Helmholtz cooling phase of the neutron star, (i) the global characteristics of the neutrino flux, e.g., luminosity and energy distribution, change rather slowly; (ii) the properties of the neutron star, e.g., mass, radius, and surface temperature, also evolve very slowly; and (iii) the supernova shock wave is at very large radii, and has little influence on the conditions close to the neutron star.

Such is the ideal world. In fact, the real local situation in the wind may be more complex. Woosley & Weaver (1995) find considerable mass continues to accrete onto the neutron star for several hours following its formation. Convection may also continue at some level even 10 s after the shock is launched. Rotation may lead to a breaking of spherical symmetry. However, in order to proceed, we shall adopt the steady-state assumption, in which case the dynamic equations can be written as (Duncan et al. 1986):

$$\dot{M} = 4\pi r^2 \rho v, \tag{1}$$

$$v\frac{dv}{dr} = -\frac{1}{\rho}\frac{dP}{dr} - \frac{GM}{r^2}, \tag{2}$$

$$\dot{q} = v\left(\frac{d\epsilon}{dr} - \frac{P}{\rho^2}\frac{d\rho}{dr}\right), \tag{3}$$

where ρ is the rest mass density, v is the outflow velocity, T is the temperature, P and ϵ are the total pressure and specific internal energy corresponding to non-relativistic matter and relativistic particles in the outflow, respectively, $\dot{q}$ is the net specific heating rate due to neutrino interactions above the neutron star, M is the mass of the neutron star, and $\dot{M}$ is the constant mass outflow rate in the ejecta. In writing the above equations, we have made the following assumptions: (i) the outflow velocity is non-relativistic; (ii) the general relativistic effects above the neutron star are small; and (iii) the neutron star is the predominant source of gravity. We will discuss the validity of these assumptions later.

As we will see in §3 and §4, the characteristics of the neutrino-driven wind are mostly determined at $T \gtrsim 0.5$ MeV. At these temperatures, the material is composed of non-relativistic free neutrons and protons, relativistic electrons and positrons, and photon radiation. The expression for pressure, P, and internal energy, ϵ, can then be approximately written as

$$P = \frac{11\pi^2}{180}T^4\left(1 + \frac{30\eta^2}{11\pi^2} + \frac{15\eta^4}{11\pi^4}\right) + \frac{\rho}{m_N}T, \tag{4}$$

$$\epsilon = \frac{11\pi^2}{60}\frac{T^4}{\rho}\left(1 + \frac{30\eta^2}{11\pi^2} + \frac{15\eta^4}{11\pi^4}\right) + \frac{3}{2}\frac{T}{m_N}, \tag{5}$$

where m_N is the nucleon rest mass, and $\eta = \mu/T$ is the degeneracy parameter with μ the electron chemical potential. The degeneracy parameter, η, is related to the electron fraction Y_e through

$$Y_e = \frac{T^3}{(\rho/m_N)} \frac{\eta}{3} \left(1 + \frac{\eta^2}{\pi^2}\right). \tag{6}$$

In equations (4) to (6), we have used the units in which the Planck constant $\hbar$, the speed of light c, and the Boltzmann constant k are taken to be unity. It is easy to obtain the correct dimension of a physical quantity if one knows that $\hbar c = 197.33$ MeV fm. For example, equation (6) in normal units would be $Y_e = (kT/\hbar c)^3 (m_N/\rho)(\eta/3)(1 + \eta^2/\pi^2)$.

The electron fraction Y_e is, in turn, determined by

$$v\frac{dY_e}{dr} = \lambda_{\nu_e n} + \lambda_{e^+ n} - (\lambda_{\nu_e n} + \lambda_{e^+ n} + \lambda_{\bar{\nu}_e p} + \lambda_{e^- p})Y_e, \tag{7}$$

where $\lambda_{\nu_e n}$, $\lambda_{\bar{\nu}_e p}$, $\lambda_{e^+ n}$, and $\lambda_{e^- p}$ are the rates for the forward and reverse reactions in the following equations:

$$\nu_e + n \;\rightleftharpoons\; p + e^-, \tag{8a}$$

$$\bar{\nu}_e + p \;\rightleftharpoons\; n + e^+. \tag{8b}$$

Given the input neutrino physics (i.e., the expressions of $\dot{q}$, $\lambda_{\nu_e n}$, $\lambda_{\bar{\nu}_e p}$, $\lambda_{e^+ n}$, and $\lambda_{e^- p}$), the initial conditions at the neutron star surface, and the boundary conditions at the shock wave, we can think of equations (1) through (7) as a complete set of equations for an "eigenvalue" problem of $\dot{M}$ in the neutrino-driven wind. Sometimes it is convenient to think of these equations as describing a Lagrangian mass element moving away from the neutron star with velocity $v(r)$. In this case, we can introduce a time variable $t = \int_{r_0}^r dr/v(r)$, with r_0 being some initial reference radius. Then the derivative with respect to t is equivalent to $v(d/dr)$.

3.   Analytic description of the neutrino-driven wind

It is helpful to estimate the general conditions before a detailed description of the neutrino-driven wind. The ejecta leave the neutron star surface with a small, very subsonic initial velocity. In order to escape to large radii, a nucleon has to gain enough energy from the neutrino flux to overcome its gravitational potential at the neutron star surface. For a typical neutron star, the mass is $M \sim 1.4 \ M_\odot$, and the radius is $R \sim 10$ km. The amount of energy provided by neutrino heating for a nucleon has to be at least $\sim GMm_N/R \sim 200$ MeV. Because the neutrino flux decreases as r^{-2} away from the neutron star, we expect that most of the heating takes place close to the neutron star. The surface temperature of a nascent neutron star is several MeV, and the thermal kinetic energy of a nucleon close to the neutron star is of the same order. Since the initial velocity of the nucleon is also small, the nucleon is incapable of carrying the amount of energy obtained from the neutrino flux. Almost all of this energy has to go into photon radiation and relativistic electron-positron pairs. This is consistent with the neutrino heating processes. In absorption of ν_e and $\bar{\nu}_e$, essentially all the neutrino energy goes into the produced electron or positron. Neutrino-antineutrino annihilation produces electron-positron pairs, and neutrino-electron scattering also transfers neutrino energy directly to electrons and positrons. Therefore, the ejecta become radiation-dominated a short distance above the neutron star. The energy initially stored in photon radiation and electron-positron pairs is converted into the mechanical energy of the nucleons at much larger radii where temperatures are low.

In terms of the local thermodynamic conditions, the dominance of radiation means that $T^3 \gg \rho/m_N$ and $\eta \ll 1$. This is clear from equations (4) to (6). Under these conditions, it is convenient to introduce a thermodynamic quantity

$$S = \frac{11\pi^2}{45} \frac{T^3}{(\rho/m_N)} \approx 5.21 \frac{T_{\mathrm{MeV}}^3}{\rho_8}, \tag{9}$$

where T_{MeV} is the temperature in MeV, and ρ_8 is the density in 10^8 g cm^{-3}. It is easy to see from equations (4) to (6) that S is the entropy per baryon in relativistic particles for $\eta = 0$. The ejecta become radiation-dominated when $S \gg 1$.

3.1. Input neutrino physics

We now calculate the heating and cooling rates resulting from interactions between the neutrino flux and material in the ejecta. We assume that neutrinos are emitted from a neutrinosphere with radius R_ν. At radius $r > R_\nu$, one only sees neutrinos within the solid angle subtended by the neutrinosphere at this radius. Because the neutrino interaction cross sections have a power law dependence on neutrino energy, the heating rates can be cast in terms of the neutrino luminosity and various neutrino energy moments, without specifying a particular neutrino energy distribution. Our approach here thus parallels pioneering analytic calculations of the supernova mechanism by Bethe (e.g., 1993).

The most important heating and cooling processes are those given in equations (8a) and (8b), i.e., neutrino absorption and electron capture on free nucleons. The specific heating rate due to neutrino absorption is

$$
\begin{aligned}
\dot{q}_{\nu N} &= \dot{q}_{\nu_e n} + \dot{q}_{\bar{\nu}_e p} \\
&\approx 9.65 N_A \left[(1 - Y_e) L_{\nu_e,51} \varepsilon_{\nu_e,\mathrm{MeV}}^2 + Y_e L_{\bar{\nu}_e,51} \varepsilon_{\bar{\nu}_e,\mathrm{MeV}}^2 \right] \frac{1 - x}{R_{\nu 6}^2} \ \mathrm{MeV\ s^{-1}\ g^{-1}},
\end{aligned} \tag{10}
$$

where $x = \sqrt{1 - R_\nu^2/r^2}$ is a function of radius, N_A is the Avogadro's number, $L_{\nu,51}$ is the individual neutrino luminosity in 10^{51} erg s^{-1}, $R_{\nu 6}$ is the neutrinosphere radius in 10^6 cm, and $\varepsilon_{\nu,\mathrm{MeV}}$ is an appropriate neutrino energy ε_ν in MeV, defined through $\varepsilon_\nu^2 \equiv \langle E_\nu^3 \rangle / \langle E_\nu \rangle$, where $\langle E_\nu^n \rangle$ denotes the nth neutrino energy moment of the neutrino energy distribution. The specific cooling rate due to capture of relativistic electrons and positrons is

$$
\dot{q}_{eN} = \dot{q}_{e^- p} + \dot{q}_{e^+ n} \approx 2.27 N_A T_{\mathrm{MeV}}^6 \ \mathrm{MeV\ s^{-1}\ g^{-1}}. \tag{11}
$$

In deriving the above rates, we have neglected the neutron-proton mass difference and the Pauli blocking effects for leptons in the final state. We have also used the fact that there are almost equal numbers of relativistic electrons and positrons in the radiation-dominated ejecta.

Neutrinos of all flavors can scatter on the electrons and positrons in the ejecta. These scattering processes also contribute to the heating. The corresponding specific heating rate is

$$
\begin{aligned}
\dot{q}_{\nu e} &= \dot{q}_{\nu_e e^-} + \dot{q}_{\nu_e e^+} + \dot{q}_{\bar{\nu}_e e^-} + \dot{q}_{\bar{\nu}_e e^+} + 2(\dot{q}_{\nu_\mu e^-} + \dot{q}_{\nu_\mu e^+} + \dot{q}_{\bar{\nu}_\mu e^-} + \dot{q}_{\bar{\nu}_\mu e^+}) \\
&\approx 2.17 N_A \ \text{MeV s}^{-1} \ \text{g}^{-1} \\
&\times \ \frac{T_{\text{MeV}}^4}{\rho_8} \left(L_{\nu_e,51} \epsilon_{\nu_e,\text{MeV}} + L_{\bar{\nu}_e,51} \epsilon_{\bar{\nu}_e,\text{MeV}} + \frac{6}{7} L_{\nu_\mu,51} \epsilon_{\nu_\mu,\text{MeV}} \right) \frac{1-x}{R_{\nu 6}^2},
\end{aligned}
\tag{12}
$$

where $\epsilon_{\nu,\text{MeV}}$ is $\epsilon_\nu \equiv \langle E_\nu^2 \rangle / \langle E_\nu \rangle$ in MeV, and where we have assumed the same characteristics for the ν_μ, $\bar{\nu}_\mu$, ν_τ, and $\bar{\nu}_\tau$ fluxes. In deriving equation (12), we have also made the approximation that the average energy transfer from neutrino to electron is $E_\nu/2$ for each scattering, instead of the more accurate value $(E_\nu - 4T)/2$ found in Tubbs and Schramm (1975). This is a reasonable approximation at $T \lesssim$ a few MeV where the neutrino-electron scattering processes are expected to be most effective.

Cooling can also occur through annihilation of relativistic electron-positron pairs into $\nu_e \bar{\nu}_e$, $\nu_\mu \bar{\nu}_\mu$, and $\nu_\tau \bar{\nu}_\tau$ pairs. The corresponding specific cooling rate is

$$
\dot{q}_{e^- e^+} \approx 0.144 N_A \frac{T_{\text{MeV}}^9}{\rho_8} \ \text{MeV s}^{-1} \ \text{g}^{-1}.
\tag{13}
$$

Of course, there are other cooling processes operating through emission of neutrino-antineutrino pairs. However, electron-positron pair annihilation into neutrino-antineutrino pairs is the most important one for the radiation-dominated conditions in the ejecta.

Finally, we give the specific heating rate for neutrino-antineutrino annihilation into

electron-positron pairs:

$$
\begin{aligned}
\dot{q}_{\nu\bar{\nu}} &\approx 12.0 N_A \text{ MeV s}^{-1} \text{ g}^{-1} \\
&\times \left[L_{\nu_e,51} L_{\bar{\nu}_e,51} \left(\epsilon_{\nu_e,\text{MeV}} + \epsilon_{\bar{\nu}_e,\text{MeV}} \right) + \frac{6}{7} L_{\nu_\mu,51}^2 \epsilon_{\nu_\mu,\text{MeV}} \right] \frac{\Phi(x)}{\rho_8 R_{\nu 6}^4},
\end{aligned} \tag{14}
$$

where $\Phi(x) = (1-x)^4(x^2 + 4x + 5)$. It is also useful to give the total heating rate due to neutrino-antineutrino annihilation above the neutrinosphere:

$$
\dot{Q}_{\nu\bar{\nu}} \approx 4.85 \times 10^{45} \left[L_{\nu_e,51} L_{\bar{\nu}_e,51} \left(\epsilon_{\nu_e,\text{MeV}} + \epsilon_{\bar{\nu}_e,\text{MeV}} \right) + \frac{6}{7} L_{\nu_\mu,51}^2 \epsilon_{\nu_\mu,\text{MeV}} \right] R_{\nu 6}^{-1} \text{ erg s}^{-1}. \tag{15}
$$

The heating and cooling rates presented above correspond to the major heating and cooling mechanisms for the ejecta. From these rates, we can make the following observations:

(1) The specific heating rate due to neutrino-antineutrino annihilation decreases rapidly away from the neutrinosphere, as is evident from the expression for $\Phi(x)$. At $r \gg R_\nu$, $\Phi(x) \to (5/8) R_\nu^8 / r^8$. Physically, this is because (i) the neutrino and antineutrino fluxes decrease as r^{-2}; (ii) the chance for a neutrino to collide with an antineutrino, especially the occurrence of almost head-on collisions decreases quickly away from the neutrinosphere; and (iii) the center-of-mass energy of the neutrino-antineutrino pair, and hence, the available phase space for the produced electron-positron pair, also decrease very fast away from the neutrinosphere. Unfortunately, our prescription for the neutrino flux does not work well close to the neutrinosphere. Therefore, the rates given for this process can only be taken as a rough estimate. Extensive studies of the heating rate due to neutrino-antineutrino annihilation were carried out by Janka (1991a,b) using Monte Carlo methods. In the subsequent (sub)sections, we will discuss to what extent the simple approximations made in deriving equations (14) and (15) will affect our understanding of the neutrino-driven wind.

(2) The relative importance of neutrino-scattering and neutrino absorption can be seen from the ratio $\dot{q}_{\nu e}/\dot{q}_{\nu N} \sim (S/23)(T/T_\nu)$, where $T_\nu \sim 5$ MeV is the temperature at the

neutrinosphere. Therefore, neutrino-electron scattering become important only at high entropies.

(3) Similarly, the relative importance of the cooling processes can be gauged by the ratio $\dot{q}_{e^-e^+}/\dot{q}_{eN} \approx S/82$. However, both cooling processes have sensitive temperature dependence, and the absolute cooling rates decrease rapidly away from the neutron star surface.

3.2.   Initial conditions

We refer to the conditions at radius R, where we start our analytic treatment of the neutrino-driven wind, as the initial conditions at the neutron star surface. These conditions are closely related to the heating and cooling processes taking place in the region between the neutrinosphere at radius R_ν and the neutron star surface at radius R. In this region, the heating and cooling processes between the intense neutrino flux and material at high temperature and density proceed at very high rates. This results in a kinetic equilibrium between the neutrino flux and the material (Burrows & Mazurek 1982), and the temperature in this region almost stays constant.

The material in this region is also in close hydrostatic equilibrium, and we have

$$-\frac{1}{\rho}\frac{dP}{dr} \approx \frac{GM}{r^2}. \tag{16}$$

For slowly varying temperature,

$$\frac{dP}{dr} \approx \frac{\rho T_\nu}{m_N}\left(Y_e\frac{d\eta}{dr} + \frac{1}{\rho}\frac{d\rho}{dr}\right). \tag{17}$$

Because previous deleptonization has led to $Y_e \ll 0.5$ at the neutrinosphere, we can neglect the first term in the above equation, and obtain

$$\rho(r) \approx \rho(R_\nu)\exp\left(-\frac{GMm_N}{R_\nu T_\nu}\frac{r - R_\nu}{R_\nu}\right) \tag{18}$$

for $r - R_\nu \ll R_\nu$. Taking $M \sim 1.4 M_\odot$, $R_\nu \sim 10$ km, and $T_\nu \sim 5$ MeV, we see that the density decreases by one e-fold over a distance scale $\sim R_\nu^2 T_\nu / GM m_N \sim 0.25$ km. As a result, the entropy in relativistic particles $S \propto T^3/\rho$ quickly rises.

The pressure and specific internal energy of the material become dominated by contributions from the relativistic particles when $S \gtrsim 4$. At this point, the temperature has to decrease sufficiently fast to break the kinetic equilibrium in order to maintain the approximate hydrostatic equilibrium. The cooling rates decrease with the falling temperature, and net heating takes place to drive a mass outflow, and to further increase the entropy. This picture is then consistent with our expectation of the general radiation-dominated condition in the ejecta.

Our initial conditions then correspond to the last radius where kinetic equilibrium can still be maintained. At this radius R, $S \gtrsim 4$, so the dominant cooling process is electron capture on free nucleons. Since the rate for this process has a sharp temperature dependence, the temperature T_i at radius R is relatively insensitive to the uncertainties in the rates for the counteracting heating processes. We can then take neutrino absorption on free nucleons as the dominant heating process, and further approximate the corresponding rate in equation (10) as

$$\dot{q}_{\nu N} \approx 2.75 N_A (L_{\nu_e,51} \epsilon_{\nu_e,\text{MeV}}^2 + L_{\bar{\nu}_e,51} \epsilon_{\bar{\nu}_e,\text{MeV}}^2) r_6^{-2} \text{ MeV s}^{-1} \text{ g}^{-1}. \tag{19}$$

In deriving the above rate, we have made the following approximations: (i) $Y_e \approx 0.5$; (ii) $1 - x \approx (1/2) R_\nu^2/r^2$; and (iii) $\varepsilon_\nu^2 \approx 1.14 \epsilon_\nu^2$. The last approximation follows from the observation that $\langle E_\nu^3 \rangle \langle E_\nu \rangle / \langle E_\nu^2 \rangle^2$ ranges from $25/24$ to $5/4$ for neutrino energy distributions of the form $f(E_\nu) \propto E_\nu^2 / [\exp(aE_\nu + b) + 1]$ with $a > 0$ and $-\infty < b < \infty$. The temperature T_i at radius R is then

$$T_i \approx 1.03 \left[1 + \frac{L_{\nu_e}}{L_{\bar{\nu}_e}} \left(\frac{\epsilon_{\nu_e}}{\epsilon_{\bar{\nu}_e}} \right)^2 \right]^{1/6} \frac{L_{\bar{\nu}_e,51}^{1/6}}{R_6^{1/3}} \epsilon_{\bar{\nu}_e,\text{MeV}}^{1/3} \text{ MeV}. \tag{20}$$

For $L_{\bar{\nu}_e} \approx 10^{51}$ erg s^{-1}, $\epsilon_{\bar{\nu}_e} \approx 20$ MeV, $L_{\nu_e}/L_{\bar{\nu}_e} \approx 1$, $\epsilon_{\nu_e}/\epsilon_{\bar{\nu}_e} \approx 0.5$–1, and $R \approx 10^6$ cm, we have $T_i \approx 3$ MeV.

We can now compare the rates $\dot{q}_{\nu e}$ and $\dot{q}_{\nu\bar{\nu}}$ with $\dot{q}_{\nu N}$. As we have discussed in §3.1, $\dot{q}_{\nu e}/\dot{q}_{\nu N} \approx (S/23)(T_i/T_\nu)$. For $S \gtrsim 4$ and $T_i \lesssim T_\nu$, $\dot{q}_{\nu e}/\dot{q}_{\nu N} \approx 1/6$. Taking $L_{\nu_e} \approx L_{\bar{\nu}_e} \approx L_{\nu_\mu} \approx 10^{51}$ erg s^{-1} and $R \approx R_\nu \approx 10^6$ cm, we obtain $\dot{q}_{\nu\bar{\nu}}/\dot{q}_{\nu e} \approx 27.6/T_{\mathrm{MeV}}^4 \approx 1/3$. Clearly, taking into account the contributions from neutrino-electron scattering and neutrino-antineutrino annihilation only increases T_i by a small amount. However, to guard against miscalculation of the heating rates, especially $\dot{q}_{\nu\bar{\nu}}$, we can multiply $\dot{q}_{\nu N}$ by a correction factor C. This then gives the temperature T_i at radius R as

$$T_i \approx 1.11 C^{1/6} L_{\bar{\nu}_e,51}^{1/6} \epsilon_{\bar{\nu}_e,\mathrm{MeV}}^{1/3} R_6^{-1/3} \text{ MeV}, \tag{21}$$

where we have assumed an average value for $[1 + (L_{\nu_e}/L_{\bar{\nu}_e})(\epsilon_{\nu_e}/\epsilon_{\bar{\nu}_e})^2]^{1/6}$. In the unlikely case where we have underestimated $\dot{q}_{\nu\bar{\nu}}$ by more than one order of magnitude, we note that a correction factor $C = 5$ only increases T_i by $\sim 30\%$. Equation (21) then constitutes our basic initial condition at the neutron star surface.

3.3. Analytic treatment

Before we start our analytic treatment of the neutrino-driven wind, we note that equations (1) to (3) describe the hydrodynamic and thermodynamic evolution of the ejecta, while equation (7) determines the chemical evolution of the ejecta. The former equations are coupled with the latter only through the dependence on Y_e in the equations of state (4) to (6) and the expression of $\dot{q}$. From the previous discussions in this section, we know that the ejecta become radiation-dominated immediately above the neutron star surface. Equations (4) and (5) are approximately reduced to

$$P \approx \frac{11\pi^2}{180} T^4, \tag{22}$$

$$\epsilon \;\approx\; \frac{11\pi^2}{60}\frac{T^4}{\rho}, \tag{23}$$

which are independent of Y_e. The expression of $\dot{q}$ has a weak dependence on Y_e, mainly through equation (10). We have eliminated this dependence by taking $Y_e \approx 0.5$ in §3.2. This is justified because $(1 - Y_e)L_{\nu_e}\varepsilon_{\nu_e}^2 + Y_e L_{\bar{\nu}_e}\varepsilon_{\bar{\nu}_e}^2 \approx (1/2)(L_{\nu_e}\varepsilon_{\nu_e}^2 + L_{\bar{\nu}_e}\varepsilon_{\bar{\nu}_e}^2)$ for any Y_e as long as $L_{\nu_e} \approx L_{\bar{\nu}_e}$ and $\varepsilon_{\nu_e} \sim \varepsilon_{\bar{\nu}_e}$. At any rate, we have introduced a correction factor C in §3.2 to account for the uncertainties in deriving the expression of $\dot{q}$. Therefore, we can separate the discussion of the ejecta into two almost independent parts. In this subsection, we derive the analytic expressions for the entropy, the dynamic time scale, and the mass outflow rate in the ejecta. These physical parameters are determined by equations (1) to (3). We devote §5 to a detailed analysis of the electron fraction in the ejecta.

Taking advantage of equations (22) and (23), we can rearrange equations (1) to (3) into

$$\left(v - \frac{v_s^2}{v}\right)\frac{dv}{dr} \;=\; \frac{1}{r}\left(\frac{2}{3}\frac{TS}{m_N} - \frac{GM}{r}\right) - \frac{\dot{q}}{3v}, \tag{24}$$

$$\dot{q} \;=\; v\frac{d}{dr}\left(\frac{v^2}{2} + \frac{TS}{m_N} - \frac{GM}{r}\right), \tag{25}$$

$$v\frac{dS}{dr} \;=\; \frac{\dot{q}m_N}{T}, \tag{26}$$

where v_s is the adiabatic sound speed in the ejecta, given by

$$v_s = \left(\frac{4}{3}\frac{P}{\rho}\right)^{1/2} = \left(\frac{TS}{3m_N}\right)^{1/2} \approx 5.67 \times 10^8 T_{\mathrm{MeV}}^{1/2} S^{1/2} \ \mathrm{cm \ s^{-1}}. \tag{27}$$

For a particular Lagrangian mass element, the above equations describe the evolution of its velocity, total "flow" energy, and entropy. We note that the total flow energy is given by the sum of enthalpy and mechanical energy, i.e., $\epsilon_{\mathrm{flow}} = v^2/2 + TS/m_N - GM/r$.

Given the initial conditions at the neutron star surface, i.e., T and S at radius R, we can choose any three independent equations from equations (1) to (3) and (24) to (26), and integrate these equations for various values of the mass outflow rate $\dot{M}$. The eigenvalue

of $\dot{M}$ is then selected to meet the boundary conditions at the shock wave. However, the qualitative features of the solutions to these equations can be readily obtained from equations (24) to (26).

From equations (25) and (26), we see that ϵ_{flow} and S always increase as long as $\dot{q} > 0$. Neutrino heating becomes negligible for $T \lesssim 0.5$ MeV because in the region at these temperatures, (i) free nucleons are bound into α-particles and heavier nuclei; (ii) electron-positron pairs annihilate into photons; and (iii) the neutrino flux has decreased by a factor $(R_\nu/r)^2$. Therefore, ϵ_{flow} and S reach their final values at $T \approx 0.5$ MeV. We note that equations (22) and (23) are invalid for $T \lesssim 0.5$ MeV due to the disappearance of electron-positron pairs. However, because entropy is conserved during the annihilation of electron-positron pairs into photons, we can show that after all the electron-positron pairs are gone, the correct equations to describe the ejecta are

$$\left(v - \frac{v_s^2}{v}\right)\frac{dv}{dr} = \frac{1}{r}\left(\frac{2}{3}\frac{TS_f}{m_N} - \frac{GM}{r}\right), \tag{28}$$

$$\epsilon_{\mathrm{flow},f} = \left(\frac{v^2}{2} + \frac{TS_f}{m_N} - \frac{GM}{r}\right), \tag{29}$$

$$S_f = \frac{4\pi^2}{45}\frac{T^3}{\rho}, \tag{30}$$

where $\epsilon_{\mathrm{flow},f}$ and S_f are the final values of ϵ_{flow} and S at $T \approx 0.5$ MeV, respectively, and $v_s = (TS_f/3m_N)^{1/2}$.

The behavior of v is more complicated. At the neutron star surface, we have $v \ll v_s$ and $\epsilon_{\mathrm{flow}} \approx -GM/R$. According to equation (24), v always increases initially. The subsequent evolution of v depends on the mass outflow rate $\dot{M}$. Given the initial conditions at the neutron star surface, the initial velocity is proportional to $\dot{M}$. For small values of $\dot{M}$, the ejecta move slowly and there is more time for the ejecta to gain energy from the neutrino flux. The right-hand side of equation (24) can become zero due to the increase in ϵ_{flow} before v reaches v_s. When this occurs, $dv/dr = 0$, and v reaches its maximum value. The velocity

decreases afterwards as the right-hand side of equation (24) becomes positive. In this case, the ejecta are always subsonic. When $\dot{M}$ increases, it can happen that the right-hand side of equation (24) becomes zero at the same time as v reaches v_s. This case corresponds to a critical value $\dot{M}_{\mathrm{crit}}$ of $\dot{M}$. In this critical case, the velocity increases through the sound speed to supersonic values, and eventually becomes a constant when all the flow energy is converted into the mechanical kinetic energy. Mass outflow rates larger than $\dot{M}_{\mathrm{crit}}$ are unphysical, because for these values of $\dot{M}$, v will reach v_s when the right-hand side of equation (24) is still negative, resulting in an unphysical infinite acceleration. Therefore, we only need to focus our attention on cases of $\dot{M} \leq \dot{M}_{\mathrm{crit}}$.

From equations (1) and (30), we see that $\rho \propto r^{-2}$ and $T \propto r^{-2/3}$ as v approaches its final value in the critical case. Therefore, $\dot{M}_{\mathrm{crit}}$ can only correspond to vanishing boundary conditions at large radii. On the other hand, in the cases of $\dot{M} < \dot{M}_{\mathrm{crit}}$, one can impose a boundary pressure, or equivalently a boundary temperature, in the radiation-dominated ejecta. The supernova shock wave at large radii can be regarded as such a boundary condition. As T in the ejecta approaches the boundary temperature T_b, ρ also approaches a constant value, and v decreases as r^{-2}, according to equations (1) and (30). However, for $T_b \ll 0.5$ MeV, there is little difference between the subsonic structures of the ejecta for the critical and subcritical mass outflow rates.

In the subcritical case, $v < v_s$ everywhere, and we can approximate equation (29) as

$$\frac{TS_f}{m_N} - \frac{GM}{r} \approx \epsilon_{\mathrm{flow},f} \approx \frac{T_b S_f}{m_N}. \tag{31}$$

In particular, this equation is also satisfied at $T \approx 0.5$ MeV because $\epsilon_{\mathrm{flow},f}$ corresponds to the flow energy at $T \approx 0.5$ MeV. If $T_b \ll 0.5$ MeV, we can take

$$\frac{TS_f}{m_N} \approx \frac{GM}{r} \quad \text{at } T \approx 0.5 \text{ MeV} \tag{32}$$

as an effective boundary condition. In the critical case, we have $(2/3)TS_f/m_N = GM/r$

when $v = v_s$. Equation (29) then gives

$$\frac{v^2}{2} + \frac{TS_f}{m_N} - \frac{GM}{r} = \epsilon_{\text{flow},f} \approx \frac{T_s S_f}{2m_N}, \tag{33}$$

where T_s is the temperature when v reaches v_s. If $T_s \ll 0.5$ MeV, i.e., $T \approx 0.5$ MeV belongs to the subsonic region, we obtain the same effective boundary condition as in equation (32). Therefore, the mass outflow rates are close to $\dot{M}_{\text{crit}}$ for small boundary temperatures, resulting in similar subsonic structures to that in the critical case. Typical boundary temperatures for the supernova shock wave are $T_b \sim 0.1$ MeV. Therefore, the mass outflow rate in the neutrino-driven wind corresponds to the effective boundary condition in equation (32). As we have stated before, our discussion of the physical conditions in the ejecta can be limited to the region at $T \gtrsim 0.5$ MeV.

The above discussion of the neutrino-driven wind is mainly based on equations (24) to (26). Strictly speaking, these equations are valid only when $S \gg S_N$, where

$$S_N \approx 11 + \ln\left(\frac{T_{\text{MeV}}^{3/2}}{\rho_8}\right) \tag{34}$$

is the entropy per baryon in non-relativistic nucleons. The number 11 in the above expression for S_N could be 12 if one distinguishes between neutrons and protons, and takes account of their spin states. However, the qualitative features given in the above discussion apply to the neutrino-driven wind as long as the pressure P and the specific energy ϵ are dominated by the contributions from electron-positron pairs and photon radiation, i.e., $S > 4$. In this case, the analytic treatments of the neutrino-driven wind are very similar for both cases of $S \gg S_N$ and $S \lesssim S_N$, if we use the general forms of equations (25) and (26):

$$\dot{q} = v\frac{d}{dr}\left(\frac{v^2}{2} + \frac{TS}{m_N} + \frac{5}{2}\frac{T}{m_N} - \frac{GM}{r}\right), \tag{35}$$

$$\frac{\dot{q}m_N}{T} = v\frac{d}{dr}\left(S + S_N\right). \tag{36}$$

Equations (35) and (36) can be easily derived from equations (2) to (5) with the approximation $\eta \ll 1$.

3.3.1.   Entropy per baryon

We first derive the final entropy S_f in the ejecta. From equation (35), we have

$$\frac{GM}{R} \approx \epsilon_{\text{flow},f} - \epsilon_{\text{flow},i} = \int_R \dot{q}\frac{dr}{v}, \tag{37}$$

where we have used the effective boundary condition in equation (32) and have taken the initial flow energy to be $\epsilon_{\text{flow},i} \approx -GM/R$. From equation (36), we have

$$S_f \approx \int_R \frac{\dot{q}m_N}{T}\frac{dr}{v} \text{ for } S_f \gg S_N, \tag{38a}$$

$$S_f \approx \frac{1}{2}\int_R \frac{\dot{q}m_N}{T}\frac{dr}{v} \text{ for } S_f \lesssim S_N. \tag{38b}$$

We can define an effective temperature T_{eff} through

$$T_{\text{eff}}^{-1} = \frac{\int_R (\dot{q}/T)(dr/v)}{\int_R \dot{q}(dr/v)} = \frac{\int_R (\dot{q}/T)dt}{\int_R \dot{q}dt}, \tag{39}$$

or equivalently,

$$S_f \approx \frac{GMm_N}{RT_{\text{eff}}} \text{ for } S_f \gg S_N, \tag{40a}$$

$$S_f \approx \frac{GMm_N}{2RT_{\text{eff}}} \text{ for } S_f \lesssim S_N. \tag{40b}$$

We can regard equation (39) as defining T_{eff}^{-1} by weighing T^{-1} over $\dot{q}$, and expect T_{eff} approximately corresponds to the temperature at which $\dot{q}$ reaches the maximum value.

Taking $\dot{q} \approx C\dot{q}_{\nu N} - \dot{q}_{eN} \propto T_i^6(R/r)^2 - T^6$, we find

$$T^5\frac{dT}{dr} = -\frac{1}{3}T_i^6\frac{R^2}{r^3} \tag{41}$$

at T_{eff}, where we have used the same correction factor introduced in equation (21) to crudely account for the heating processes other than neutrino absorption on free nucleons. We note that in general this correction factor C should vary with radius, for example, due to the increasing importance of $\dot{q}_{\nu e}$ relative to $\dot{q}_{\nu N}$ at higher entropies. However, for the

purpose of simple analytic treatments, we will take C to be constant and subsequently derive its suitable value to be used in the analytic estimates for the entropy per baryon, the dynamic time scale, and the mass outflow rate in the wind.

Because hydrostatic equilibrium approximately holds in the subsonic region, we have

$$\frac{1}{\rho}\frac{dP}{dr} = \beta\frac{S}{m_N}\frac{dT}{dr} \approx -\frac{GM}{r^2}, \tag{42}$$

where we have introduced a numerical factor β to account for the contribution to P from non-relativistic free nucleons. For $S_f \gg S_N$, $\beta \approx 1$, and for $S_f \lesssim S_N$, $\beta \approx 2$. Equations (41) and (42) then give

$$T_{\text{eff}} = T_i\left(\frac{\beta}{3}\frac{T_{\text{eff}}S_{\text{eff}}r_{\text{eff}}}{GMm_N}\right)^{1/6}\left(\frac{R}{r_{\text{eff}}}\right)^{1/3}, \tag{43}$$

where r_{eff} and S_{eff} are the radius and entropy, respectively, corresponding to T_{eff}. Hereafter, we use the subscript "eff" to denote parameters at the radius where $\dot{q}$ reaches the maximum value. To proceed further, we make the following approximation:

$$S_{\text{eff}} \approx \frac{S_f}{2}, \tag{44}$$

and

$$T_{\text{eff}}S_{\text{eff}} \approx \frac{GMm_N}{2r_{\text{eff}}}. \tag{45}$$

The numerical factors in equations (44) and (45) are conveniently chosen to reflect that the concerned quantities at r_{eff} are in the "middle" of some characteristic evolution. Using equations (40a), (40b), (44), and (45), we find

$$r_{\text{eff}} \approx R \text{ for } S_f \gg S_N, \tag{46a}$$

$$r_{\text{eff}} \approx 2R \text{ for } S_f \lesssim S_N. \tag{46b}$$

Substituting equations (45), (46a), and (46b) into equation (43), we have

$$T_{\text{eff}} \approx 6^{-1/6}T_i \text{ for } S_f \gg S_N, \tag{47a}$$

$$T_{\text{eff}} \approx 12^{-1/6}T_i \text{ for } S_f \lesssim S_N. \tag{47b}$$

Combining equations (21), (40a), (40b), (47a), and (47b), we obtain

$$S_f \approx 235 C^{-1/6} L_{\bar{\nu}_e,51}^{-1/6} \epsilon_{\bar{\nu}_e,\text{MeV}}^{-1/3} R_6^{-2/3} \left(\frac{M}{1.4 M_\odot} \right) \text{ for } S_f \gg S_N, \qquad (48a)$$

$$S_f \approx 132 C^{-1/6} L_{\bar{\nu}_e,51}^{-1/6} \epsilon_{\bar{\nu}_e,\text{MeV}}^{-1/3} R_6^{-2/3} \left(\frac{M}{1.4 M_\odot} \right) \text{ for } S_f \lesssim S_N. \qquad (48b)$$

The total entropy per baryon S_{tot} in the ejecta is

$$S_{\text{tot}} \approx S_f + S_N \approx S_f + \ln S_f + 10, \qquad (49)$$

where we have evaluated S_N at $T \approx 0.5$ MeV using S_f and taking advantage of the logarithmic dependence of S_N on T.

We can also derive an approximate value for the correction factor C. Assuming that the main heating process other than neutrino absorption on free nucleons is neutrino-electron scattering, we can take the correction factor to be

$$C \approx 1 + \frac{\dot{q}_{\nu e,\text{eff}}}{\dot{q}_{\nu N,\text{eff}}}. \qquad (50)$$

From equations (12) and (19), we obtain

$$\frac{\dot{q}_{\nu e,\text{eff}}}{\dot{q}_{\nu N,\text{eff}}} \approx 7.33 R_6^{-1} \left(\frac{M}{1.4 M_\odot} \right) \frac{\epsilon_{\nu_e,\text{MeV}} + \epsilon_{\bar{\nu}_e,\text{MeV}} + (6/7)\epsilon_{\nu_\mu,\text{MeV}}}{\epsilon_{\nu_e,\text{MeV}}^2 + \epsilon_{\bar{\nu}_e,\text{MeV}}^2} \text{ for } S_f \gg S_N, \quad (51a)$$

$$\frac{\dot{q}_{\nu e,\text{eff}}}{\dot{q}_{\nu N,\text{eff}}} \approx 3.66 R_6^{-1} \left(\frac{M}{1.4 M_\odot} \right) \frac{\epsilon_{\nu_e,\text{MeV}} + \epsilon_{\bar{\nu}_e,\text{MeV}} + (6/7)\epsilon_{\nu_\mu,\text{MeV}}}{\epsilon_{\nu_e,\text{MeV}}^2 + \epsilon_{\bar{\nu}_e,\text{MeV}}^2} \text{ for } S_f \lesssim S_N, \quad (51b)$$

where we have used equations (45), (46a), and (46b) to evaluate T^4/ρ in equation (12), and where we have assumed $L_{\nu_e} \approx L_{\bar{\nu}_e} \approx L_{\nu_\mu}$. Typically, we have $\epsilon_{\nu_e} + \epsilon_{\bar{\nu}_e} \approx \epsilon_{\nu_\mu}$, $\epsilon_{\nu_e} \approx (0.5\text{–}1)\epsilon_{\bar{\nu}_e}$, and $\epsilon_{\bar{\nu}_e} \approx 20$ MeV. So numerically, $[\epsilon_{\nu_e,\text{MeV}} + \epsilon_{\bar{\nu}_e,\text{MeV}} + (6/7)\epsilon_{\nu_\mu,\text{MeV}}]/(\epsilon_{\nu_e,\text{MeV}}^2 + \epsilon_{\bar{\nu}_e,\text{MeV}}^2) \approx 0.1$.

3.3.2. Mass outflow rate

Next, we derive the mass outflow rate $\dot{M}$ in the ejecta. The total net neutrino heating rate above $r_{\rm eff}$ is given by

$$\int_{r_{\rm eff}} \dot{q}\frac{dr}{v} \approx C\int_{r_{\rm eff}} \dot{q}_{\nu N,i}\frac{R^2}{r^2}\frac{dr}{v} \approx C\dot{q}_{\nu N,i}\frac{4\pi R^2}{\dot{M}}\int_{r_{\rm eff}} \rho dr, \tag{52}$$

where

$$C\dot{q}_{\nu N,i} \approx 2.27 N_A T_{i,\rm MeV}^6 \text{ MeV s}^{-1}\text{ g}^{-1} \approx 2.19\times 10^{18} T_{i,\rm MeV}^6 \text{ erg s}^{-1}\text{ g}^{-1}. \tag{53}$$

To estimate the integral in equation (52), we need the density scale height $h_{\rho,\rm eff}$ at $r_{\rm eff}$. We can relate $h_{\rho,\rm eff}$ to the corresponding temperature scale height $h_{T,\rm eff}$ by

$$h_{\rho,\rm eff} \approx h_{T,\rm eff}/3, \tag{54}$$

for the radiation-dominated ejecta ($S \gtrsim 4$). In turn, $h_{T,\rm eff}$ can be estimated from equation (42) as

$$h_{T,\rm eff} = \left|\frac{d\ln T}{dr}\right|_{\rm eff}^{-1} \approx \beta\frac{r_{\rm eff}^2 T_{\rm eff} S_{\rm eff}}{GMm_N}. \tag{55}$$

Now the integral in equation (52) can be approximated as

$$\int_{r_{\rm eff}} \rho dr \approx \rho_{\rm eff} h_{\rho,\rm eff} \approx \frac{11\pi^2}{135}\beta\frac{T_{\rm eff}^4 r_{\rm eff}^2}{GM}, \tag{56}$$

where we have used equation (9) to express $\rho_{\rm eff}$ in terms of $T_{\rm eff}$ and $S_{\rm eff}$.

From equation (35), we have

$$\epsilon_{{\rm flow},f} - \epsilon_{\rm flow,eff} \approx \frac{1}{2}\frac{GM}{r_{\rm eff}} \approx \int_{r_{\rm eff}} \dot{q}\frac{dr}{v}, \tag{57}$$

where we have used equation (45) to evaluate $\epsilon_{\rm flow,eff}$. Combining equations (52), (53), (56), and (57), we obtain

$$\dot{M} \approx 1.14\times 10^{-10} C^{5/3} L_{\bar{\nu}_e,51}^{5/3}\epsilon_{\bar{\nu}_e,\rm MeV}^{10/3} R_6^{5/3}\left(\frac{1.4M_\odot}{M}\right)^2 M_\odot\text{ s}^{-1}, \text{ for } S_f \gg S_N, \tag{58a}$$

$$\dot{M} \approx 1.15\times 10^{-9} C^{5/3} L_{\bar{\nu}_e,51}^{5/3}\epsilon_{\bar{\nu}_e,\rm MeV}^{10/3} R_6^{5/3}\left(\frac{1.4M_\odot}{M}\right)^2 M_\odot\text{ s}^{-1}, \text{ for } S_f \lesssim S_N, \tag{58b}$$

where we have also used equations (21), (46a), (46b), (47a), and (47b). The total power of net neutrino heating $\dot{Q} \approx GM\dot{M}/R$ is approximately given by

$$\dot{Q} \approx 4.25 \times 10^{43} C^{5/3} L_{\bar{\nu}_e,51}^{5/3} \epsilon_{\bar{\nu}_e,\mathrm{MeV}}^{10/3} R_6^{2/3} \left(\frac{1.4M_\odot}{M}\right) \mathrm{erg\ s^{-1}} \mathrm{\ for\ } S_f \gg S_N, \qquad (59a)$$

$$\dot{Q} \approx 4.28 \times 10^{44} C^{5/3} L_{\bar{\nu}_e,51}^{5/3} \epsilon_{\bar{\nu}_e,\mathrm{MeV}}^{10/3} R_6^{2/3} \left(\frac{1.4M_\odot}{M}\right) \mathrm{erg\ s^{-1}} \mathrm{\ for\ } S_f \lesssim S_N. \qquad (59b)$$

3.3.3. Dynamic time scale

Finally, we derive the dynamic time scale in the ejecta. We define this time scale to be

$$\tau_{\mathrm{dyn}} \equiv \left.\frac{r}{v}\right|_{T \approx 0.5 \mathrm{\ MeV}}. \qquad (60)$$

From equations (1), (9), (32), (48a), (48b), (58a), and (58b), we find

$$\tau_{\mathrm{dyn}} \approx 68.4 C^{-1} L_{\bar{\nu}_e,51}^{-1} \epsilon_{\bar{\nu}_e,\mathrm{MeV}}^{-2} R_6 \left(\frac{M}{1.4M_\odot}\right) \mathrm{s} \qquad (61)$$

for both cases of $S_f \gg S_N$ and $S_f \lesssim S_N$. The time scale derived in equation (61) will prove important for heavy element nucleosynthesis in the neutrino-driven wind. We illustrate its usefulness as follows.

We expect $GMm_N/r \approx TS_f$, or equivalently $T \propto r^{-1}$, to approximately hold between $T \approx 0.5$ MeV and $T \gtrsim T_b \sim 0.1$ MeV. If we ignore the effect of annihilation of electron-positron pairs into photons, we roughly have $S_f \propto T^3/\rho$ and $\rho \propto r^{-3}$, which leads to $v \propto r$ for a constant mass outflow rate $\dot{M} = 4\pi r^2 \rho v$. Therefore, the time for the temperature to decrease from $T \approx 0.5$ MeV to, say 0.2 MeV, is $\sim \tau_{\mathrm{dyn}} \ln(0.5/0.2) \sim \tau_{\mathrm{dyn}}$.

Between the radius where the temperature reaches $T \approx T_b \sim 0.1$ MeV for the first time and the position of the shock wave, both the temperature and density of the ejecta remain

approximately constant. According to $\dot{M} = 4\pi r^2 \rho v$, we have $v \propto r^{-2}$, from which the time dependence of the radius for a particular Lagrangian mass element can be obtained with $r/v \sim \tau_{\rm dyn}$ at the initial radius for $T \approx T_b$.

To summarize, we have derived the total entropy per baryon, the mass outflow rate, and the relevant dynamic time scale for heavy element nucleosynthesis in the neutrino-driven wind. In particular, we have shown that these physical conditions for heavy element nucleosynthesis only depend on the neutrino luminosity and energy distributions, and the mass and radius of the neutron star.

4. Numerical runs using KEPLER

In order to test some of the approximations derived in the previous section, a series of calculations were carried out using the one-dimensional implicit hydrodynamic code, KEPLER (Weaver, Zimmerman, & Woosley 1978). This Lagrangian-coordinate-based code has an appropriate equation of state for the ions, radiation, electrons, and pairs under all conditions of interest here. For example, this equation of state adequately treats electrons in any arbitrarily relativistic and degenerate regime. It is most important that the code is implicitly differenced and thus capable of accurately following the evolution in a situation where, as here, tight hydrostatic equilibrium exists. Though the code has provision for radiation transport, energy transport other than by neutrinos is negligible here. Only the outer layers of the neutron star were carried, approximately 0.01 $M_\odot$. The remainder of the neutron star was represented by a boundary condition of given radius, gravitational potential, and neutrino luminosity. Typical densities and temperatures at the basis of the problem were 10^{13} g cm^{-3} and 8–10 MeV. The wind of course originated at much lower densities and temperatures in a small amount of mass.

Also important was the code's ability to smoothly and repeatedly rezone the material in the wind as its density decreased. Typical zoning in the wind was about $10^{-8} M_\odot$. The velocity structure and, in the asymptotic region, the mass outflow rate, $\dot{M} = 4\pi r^2 \rho v$, were, at all times following a start-up transient, well behaved and smooth.

On the other hand, the neutrino physics employed was primitive by the standard of modern supernova codes. The inner boundary acted as a "light bulb" and the overlying layers were assumed to subtract nothing from the flux, i.e., the optically thin limit was assumed. The neutrino luminosity was shared equally among the six varieties and each neutrino species was characterized by its mean energy and flux. For a neutrinosphere radius of $R_\nu = 10$ km (also the approximate neutron star radius, R), the assumed mean energies were $\epsilon_\nu \equiv \langle E_\nu^2 \rangle / \langle E_\nu \rangle = 12, 22, 34$ MeV for ν_e, $\bar{\nu}_e$, and ν_μ, respectively. The corresponding values for $R_\nu = 30$ km were 16, 20, 32 MeV. These neutrinos could interact with nucleons and pairs (and with one another) in the neutron star crust and wind according to equations (10), (11), (12), and (14). Neutrino losses due to pair annihilation, plus plasma and photoneutrino processes were calculated separately assuming $Y_e \approx 0.50$ and the fitting functions of Munakata, Koyama, & Itoh (1985). This is more accurate than equation (13).

Nuclear physics, other than the neutrino interactions, was very simple. Since in the region of interest, nuclear statistical equilibrium (NSE) exists and the composition is solely neutrons, protons, and α-particles, only these three constituents were carried. Since the neutrino interactions with the two nucleon species are similar only one species was carried. The transition from nucleons to α-particles, which effectively shuts off the neutrino-nucleon interaction (neutrino-electron scattering and neutrino-antineutrino annihilation still contribute) was approximated using the following prescription for the free nucleon mass fraction:

$$X_N \approx 828 \frac{T_{\mathrm{MeV}}^{9/8}}{\rho_8^{3/4}} \exp(-7.074/T_{\mathrm{MeV}}) \tag{62}$$

or unity, whichever was the smaller (Woosley & Baron 1992). The free nucleon mass fraction X_N given by this prescription was used to multiply the rates in equations (10) and (11) to give the capture rates of neutrinos and pairs on nucleons.

4.1. Newtonian calculations

Nine models were then calculated. In each model the neutron star was represented by an inner boundary condition of given interior mass, radius, and neutrino luminosity. The parameters employed as well as sample results are given in Table 1 and Figs. 1 and 2.

Each model was constructed by allowing a coarsely-zoned version of the neutron star crust and atmosphere to come into approximate hydrostatic equilibrium with the inner boundary conditions. This typically took a few milliseconds. Then the zoner was turned on. Both adzoning and dezoning were employed. This acted to give smooth temperature and density profiles. Typically in the steady-state solution there were about 200 zones and about a dozen zones per decade of density in the region of interest. Typical zone masses were $10^{-8} M_\odot$ except near the inner boundary where the zoning smoothly increased on a logarithmic scale to $\sim 10^{-3} M_\odot$. Zones were removed from the surface of the problem, typically when the density had declined to about 1 g cm^{-3} so as to inhibit a runaway accumulation of zones.

Each problem was run long enough that a steady state had clearly been attained. For total neutrino luminosities of 10^{52} erg s^{-1} this took about one second. For higher luminosities, the corresponding time was about 0.2 s. Here we point out that our numerical approach to model the neutrino-driven wind differs from that of Duncan et al. (1986). Their numerical model of the neutrino-driven wind was based on the wind equations (1) to (3), and mathematically was an eigenvalue problem looking for the mass outflow rate

$\dot{M}$. In our approach, we started from some initial configuration of the material above the neutron star surface, and evolved the mass outflow into a steady-state neutrino-driven wind. Therefore, not only did we obtain the mass outflow rate $\dot{M}$ and other physical parameters in the steady state, but also showed that a steady state could actually be reached over some relaxation time scale of the problem. The relaxation time scale could then be compared with the evolution time scales of the inner boundary (especially the neutrino luminosity) to establish the quasi-steady-state nature of the neutrino-driven wind. For typical decay time of $\sim$ several seconds for the neutrino luminosity, the steady-state approximation in our analytic treatments of the neutrino-driven wind is valid.

Because the code did not include general relativistic corrections to gravity, two different baryon masses, 1.4 and 2.0 $M_\odot$, were employed for the neutron star. The smaller value is more typical of the gravitational mass of neutron stars and the baryon mass of many presupernova model calculations (e.g., Timmes, Woosley, & Weaver 1996), but the latter gives a more realistic gravitational potential, at least near the neutron star surface, when the neutron star has approximately reached its final radius of about 10 km.

Table 1 compares numerical and analytic results for the total power of net neutrino heating, the mass outflow rate, the final total entropy per baryon, and the dynamic time scale in the neutrino-driven wind. As we can see, the analytic results for these parameters agree with the numerical output from KEPLER within a factor of 2 in all nine models. The agreement between the numerical and analytic results is the best for the final entropy per baryon in the wind, as can be expected from the shallow dependence on the correction factor C in equations (48a) and (48b). This correction factor indicates the uncertainties in the analytic treatment of various neutrino heating processes. In our numerical models, neutrino absorption on free nucleons is the main heating process. Neutrino-electron scattering can make significant contribution to the heating for the cases with high entropies, i.e., the

models with $R = 10$ km. For all nine models, neutrino-antineutrino annihilation contributes at most $\sim 15\%$ to the total heating.

While the general agreement between numerical and analytic results is important to show, we also highlight the predicted power-law dependences on the neutrino luminosity and mean energy, and the mass and radius of the neutron star for the physical parameters listed in Table 1. As can be easily verified from the numerical results in Table 1, the power-law dependences on the neutrino luminosity for these physical parameters follow the analytic predictions with good accuracy.

4.2. Post-Newtonian calculations

The models of the previous subsection were all calculated using a simple Newtonian theory of gravity. A neutron star is of course a relativistic system. To zeroth order the gravity of the neutron star can simply be increased, e.g., by turning up its mass, as was done in Models 10D, 10E, and 10F. However, the actual radial dependence of gravity differs from r^{-2} in general relativity. To check that this does not have an appreciable effect on the mass outflow rate, entropy, and dynamic time scale, two additional models were calculated using a version of KEPLER modified to include first-order post-Newtonian corrections to the gravitational force (e.g., Fuller, Woosley, & Weaver 1986; Shapiro & Teukolsky 1983). The gravitational term in the force equation (Weaver, Zimmerman, & Woosley 1978), Gm_r/r^2, was replaced by

$$\frac{Gm_r}{r^2}\left(1 + \frac{P}{\rho c^2} + \frac{4\pi P r^3}{m_r c^2}\right)\left(1 - \frac{2Gm_r}{rc^2}\right)^{-1},$$

where m_r is the mass included within a radius r. The term corresponding to $\dot{q}$ in the energy equation was unchanged.

This includes the leading post-Newtonian corrections to the wind dynamics (with the wind velocity always much less than c). Unfortunately it does not include the gravitational effects on the neutrino energy spectra and angular distributions.

Models 10B and 10E were then recalculated using the modified gravitational field. The former had a neutron star mass at infinity of 1.4 $M_\odot$ and a total neutrino luminosity of 6×10^{51} erg s^{-1}. In steady state, the post-Newtonian model had a mass loss rate of 7.0×10^{-6} $M_\odot$ s^{-1}, an asymptotic entropy of 116, and a dynamic time scale of 0.044 s. Compared to quantities in Table 1, we see that the effect of the modified gravitational potential is to increase the entropy by about 1/3 (from 87 to 116) and decrease the dynamic time scale by about 1/3. The post-Newtonian version of Model 10B in fact resembles Model 10E, though perhaps an effective mass of 1.8 $M_\odot$ instead of 2 $M_\odot$ might have been more appropriate.

We also considered the extreme case of Model 10E (neutron star mass at infinity of 2.0 $M_\odot$) *and* post-Newtonian corrections. Neglecting general relativistic corrections to the neutrino transport is clearly wrong here. While allowed by causality, this is also a heavier neutron star than commonly derived in binary systems. We consider this as an example of the state a neutron star might pass through while evolving to a black hole on a Kelvin-Helmholtz cooling time scale. The asymptotic entropy for this model is 205, the mass loss rate is 2.4×10^{-6} $M_\odot$ s^{-1}, and the dynamic time scale is 0.035 s; i.e., a 60% increase in the entropy and about a factor of 2 reduction in the dynamic time scale.

In summary, the effect of post-Newtonian corrections to gravity is to increase the entropy and shorten the dynamic time scale by substantial amounts. In this regard, a stronger gravitational potential is more favorable to the r-process.

4.3. Effect of an external boundary pressure

Except in the case of the accretion-induced collapse of a neutron star the wind will not be able to flow unencumbered to infinity. It will be impeded by external matter and radiation in that portion of the supernova through which the shock has already passed.

Woosley & Weaver (1995) show that the pressure behind the shock will be largely due to radiation in a nearly isothermal sphere. At a time of several seconds this temperature is very approximately two billion K. It declines to under one billion K by the time the neutron star is 10 seconds old.

To illustrate the effect, we have recalculated Model 10E with an external boundary pressure appropriate to a temperature of 2×10^9 K. This is an extreme case; a realistic model would have less boundary pressure at 10 s. The converged model was run for one second with this boundary pressure and reached an approximate steady state though the outer boundary was being gradually pushed out at 200 km s^{-1} (corresponding to PdV work of 4×10^{46} erg s^{-1}). Figure 3 shows that there is little change in the structure of the wind, except near its outer boundary. The asymptotic entropy was increased from 129 to 140 and the mass loss rate reduced from 6.7×10^{-6} to about 6.3×10^{-6} $M_\odot$ s^{-1}. The dynamic time scale (at 0.5 MeV) was lengthened from 0.066 s to 0.11 s.

In summary, the effect of a moderate external boundary pressure is to increase the entropy slightly, and decrease the expansion rate appreciably. Overall there is little modification of the parameters of the wind in the region where the r-process occurs except that the material has a longer time to capture neutrons. The slower time scale at temperatures of 3 to 5 billion K will also give a smaller neutron-to-seed ratio in the ejecta. This is an adverse effect, but not a large one.

4.4. Effect of an artificial energy source

As Figs. 1 and 2 show, the mass outflow rate is determined closer to the neutron star than the entropy. One consequence of this is that any attempt to increase the entropy of the wind simply by raising the overall neutrino heating rate is thwarted by an increased outflow rate. The extra energy goes into doing additional work against the gravity of the neutron star and not into raising the entropy of the wind. This is also to be expected from the dependences of S and $\dot{M}$ on the neutrino luminosity and the correction factor C in equations (48a), (48b), (58a) and (58b): $S \propto (CL_\nu)^{-1/6}$ vs. $\dot{M} \propto (CL_\nu)^{5/3}$.

Conversely, energy that is added after the mass loss rate has already been determined can have a very beneficial effect, both in raising the entropy and increasing the velocity, both good for the r-process. Energy that is added too late however, after the temperature has already gone below two billion K, has little nucleosynthetic effect. The neutron-to-seed ratio for the r-process has already been set. This suggests that an additional energy source between about 20 and 50 km might have considerable leverage on the nucleosynthesis in the wind. Possible sources of this energy are discussed later in the paper (§6).

We thus explored the effect of adding an additional 10^{48} erg s^{-1} to Model 10E at a radius between 20 and 30 km. The total energy deposited thus became 4×10^{48} erg s^{-1} instead of 3×10^{48} erg s^{-1}. Of this 10^{48} erg s^{-1}, roughly 10% has a physical origin in the recombination of nucleons to α-particles ($\sim 7 \times 10^{18}$ erg g^{-1} times $\dot{M}$) . This occurs at $T \lesssim 1$ MeV or a radius of about 15–20 km.

The mass outflow rate in the modified model increased slightly from 6.7×10^{-6} $M_\odot$ s^{-1} to 9.0×10^{-6} $M_\odot$ s^{-1}, and the asymptotic entropy rose substantially, from 129 to 190. Most importantly the expansion time scale at 0.5 MeV decreased from 0.066 to 0.010 s. The velocity at 0.5 MeV was 3500 km s^{-1}. These are conditions quite favorable to the r-process

(Hoffman et al. 1996b).

Model 10F in Fig. 4 shows what a relatively small amount of energy will do if it can be generated in the right place and time. An additional volume energy term (9.7×10^{27} erg cm^{-3} s^{-1}) was added for radii between 15 and 25 km giving a total added energy of 5×10^{47} erg s^{-1}, a moderate perturbation on the 1.2×10^{48} erg s^{-1} the neutrinos were already adding. As a result, the mass loss rate increased a little to 3.7×10^{-6} $M_\odot$ s^{-1}, the entropy climbed to 192 and the dynamic time scale at 0.5 MeV shrank to 0.022 s. These conditions should be quite favorable for the r-process for $Y_e \lesssim 0.40$ (Hoffman et al. 1996b).

Larger energy deposition was not explored as it would no longer be a perturbation on the neutrino-driven wind, but the driving term for the mass loss.

4.5. Uncertainty in the neutrino energy deposition

Of the three interactions that deposit energy in the wind — neutrino capture on nucleons, neutrino scattering on electrons, and neutrino-antineutrino annihilation — the last is probably worst approximated in our calculations. The radial dependence of equation (14) is very steep. Detailed and better treatment of this dependence was given by Janka (1991a,b). Multidimensional and multi-group neutrino transport calculations by Jim Wilson (1996) show that within two neutron star radii, the approximation in equation (14) is probably a gross underestimate of the actual heating rate due to neutrino-antineutrino annihilation. Even larger deviations may be expected when a fully general relativistic transport calculation is ultimately done. The effects of general relativity on neutrino transport calculations were also discussed by Janka (1991a).

For someone seeking high entropy and rapid expansion neutrino-antineutrino annihilation has the attractive feature that it deposits energy at a rate independent of the

local matter density. It can thus boost the specific energy and entropy of a wind after its density has already declined. The problem is the steep fall-off of the neutrino-antineutrino annihilation rate with radius and its low efficiency. For Model 10E, of the 3×10^{48} erg s^{-1} being deposited in the steady-state model, about 10% is due to neutrino-antineutrino annihilation.

We thus experimented with varying the radial dependence and efficiency of neutrino-antineutrino annihilation. In one calculation Model 10E was run with an additional 10^{48} erg s^{-1} deposited as a constant volume term (3.4×10^{28} erg cm^{-3} s^{-1}) between 10 and 20 km (the surface of the neutron star and twice its radius). As a result, the asymptotic entropy increased from 129 to 137, the mass outflow rate climbed from 6.7×10^{-6} to 8.8×10^{-6} $M_\odot$ s^{-1}, and the dynamic time scale at 0.5 MeV declined from 0.066 s to 0.040 s.

A second calculation maintained the functional form of equation (14), but multiplied the neutrino-antineutrino annihilation efficiency by a factor of six inside 20 km. This resulted in increases of the energy deposition to 3.4×10^{48} erg s^{-1} and mass outflow rate to 7.8×10^{-6} $M_\odot$ s^{-1}, and decreases in entropy to 127 and dynamic time scale to 0.061 s.

Finally, we explored, again in Model 10E, changing the radial dependence of equation (14). The term $(1 - x)$ in $\Phi(x)$ was raised to the third power instead of the fourth and the overall efficiency multiplied by 3 (at all radii). This raised the energy deposition to 3.8×10^{48} erg s^{-1}, the entropy to 134, the mass outflow rate to 8.8×10^{-6} $M_\odot$ s^{-1}, and decreased the dynamic time scale to 0.044 s.

We conclude that reasonable variations in the efficiency of neutrino-antineutrino annihilation can give a modest increase in the entropy and decrease in the dynamic time scale. However, very large increases in the entropy, like a doubling, would require more radical alterations than we think are justified at the present time. Unfortunately any energy source that is peaked near the neutron star surface tends to increase the mass loss rate

more than the entropy.

4.6. A time variable neutrino luminosity?

Our analytic solutions assume a steady state in which the neutrino luminosity does not vary. In the real situation the local neutrino flux in the outflowing wind may vary considerably because of rotation, accretion, and convective flows. We thus explored the effect on Model 10E of varying the total neutrino luminosity on a time scale comparable to the flow time across the wind zone. In particular, we take the total neutrino luminosity to be $L_{\nu,\mathrm{tot}} = 6 \times 10^{51}[1 + 0.5\sin(2\pi t/\tau_\nu)]$ erg s^{-1} with $\tau_\nu = 0.1$ s. Much shorter time scales would have had no effect. Much longer time scales would have given the steady-state solutions previously described.

The chief effect of this variation in the neutrino luminosity was to cause a periodic variation in the outflow velocity and dynamic time scale. The entropy, e.g., at 0.5 MeV, did not change greatly from 129 in the steady-state model, being 127 ± 3 during three oscillations. But the outflow velocity varied almost linearly with the neutrino luminosity so that the dynamic time scale at 0.5 MeV oscillated between 0.044 and 0.15 s (the steady-state value for Model 10E was 0.066 s). A similar calculation in which $\tau_\nu = 0.2$ s gave the same range of dynamic time scales, but with an entropy oscillating between 115 and 136. In both cases the larger entropy was associated with the faster outflow. Note that an inverse dependence of the expansion time scale on the neutrino luminosity is predicted by equation (61) for the steady-state wind.

We conclude that reasonable variations in the neutrino luminosity on intervals of order 0.1 s can give a large range of expansion time scales at nearly constant entropy. Thus it is possible to have, in a fraction of the ejecta, material which has experienced the high entropy

appropriate to a low time-averaged neutrino luminosity, but with the rapid expansion time scale characteristic of the temporary peaks.

5. Electron fraction in the neutrino-driven wind

In this section, we describe how the electron fraction Y_e is determined in the neutrino-driven wind. As we will see, the final Y_e in the ejecta is principally set by the characteristics of the ν_e and $\bar{\nu}_e$ fluxes. In this regard, we also discuss general aspects of neutrino emission in supernovae, and present a novel neutrino "two-color plot" to illustrate the time evolution of the ν_e and $\bar{\nu}_e$ energy distributions. To conclude the section, we discuss the implications of this evolution plot for heavy element nucleosynthesis in supernovae.

5.1. Input neutrino physics

We begin our discussion by calculating the rates for the forward and reverse reactions in equations (8a) and (8b). These reactions are the most important processes which set the electron fraction Y_e in the neutrino-driven wind. The cross sections for the forward reactions in equations (8a) and (8b) are given by

$$\sigma_{\nu N} \approx \frac{1 + 3\alpha^2}{\pi} G_F^2 P_e E_e \approx \frac{1 + 3\alpha^2}{\pi} G_F^2 E_e^2, \tag{63}$$

where $\alpha \approx 1.26$, P_e and E_e are the momentum and total energy, respectively, of the electron or positron in the final state, and where we have made the approximation $P_e E_e \approx E_e^2$. This approximation is very good because (i) the energy of the final state electron in equation (8a) is at least the neutron-proton mass difference; and (ii) in any case, the typical neutrino

energy is about 10 MeV or more, which makes the final state electrons and positrons extremely relativistic.

Following the prescription for the neutrino flux in §3.1, we find the rates for the forward reactions in equations (8a) and (8b) to be

$$\lambda_{\nu_e n} \approx \frac{1 + 3\alpha^2}{2\pi^2} G_F^2 \frac{L_{\nu_e}}{R_\nu^2} \left(\epsilon_{\nu_e} + 2\Delta + \frac{\Delta^2}{\langle E_{\nu_e} \rangle} \right) (1 - x), \tag{64a}$$

$$\lambda_{\bar{\nu}_e p} \approx \frac{1 + 3\alpha^2}{2\pi^2} G_F^2 \frac{L_{\bar{\nu}_e}}{R_\nu^2} \left(\epsilon_{\bar{\nu}_e} - 2\Delta + \frac{\Delta^2}{\langle E_{\bar{\nu}_e} \rangle} \right) (1 - x), \tag{64b}$$

where $\Delta = 1.293$ MeV is the neutron-proton mass difference. At $r \gg R_\nu$, we can write the above rates as

$$\lambda_{\nu_e n} \approx 4.83 L_{\nu_e,51} \left(\epsilon_{\nu_e,\mathrm{MeV}} + 2\Delta_{\mathrm{MeV}} + 1.2 \frac{\Delta_{\mathrm{MeV}}^2}{\epsilon_{\nu_e,\mathrm{MeV}}} \right) r_6^{-2} \, \mathrm{s}^{-1}, \tag{65a}$$

$$\lambda_{\bar{\nu}_e p} \approx 4.83 L_{\bar{\nu}_e,51} \left(\epsilon_{\bar{\nu}_e,\mathrm{MeV}} - 2\Delta_{\mathrm{MeV}} + 1.2 \frac{\Delta_{\mathrm{MeV}}^2}{\epsilon_{\bar{\nu}_e,\mathrm{MeV}}} \right) r_6^{-2} \, \mathrm{s}^{-1}, \tag{65b}$$

where Δ_{MeV} is Δ in MeV, and where we have taken an average value of $\epsilon_\nu / \langle E_\nu \rangle = 1.2$. In fact, $\epsilon_\nu / \langle E_\nu \rangle$ ranges from $16/15$ to $4/3$ for neutrino energy distributions of the form $f(E_\nu) \propto E_\nu^2 / [\exp(a E_\nu + b) + 1]$ with $a > 0$ and $-\infty < b < \infty$. We have taken into account the neutron-proton mass difference to give accurate values of the above reaction rates. As we will see in §5.2, the final Y_e in the ejecta is sensitive to the ratio of these reaction rates.

The cross sections for the reverse reactions in equations (8a) and (8b) are given by

$$\sigma_{eN} \approx \frac{1 + 3\alpha^2}{2\pi} G_F^2 E_\nu^2, \tag{66}$$

where E_ν is the neutrino energy in the final state. The rates for these reactions are

$$\lambda_{e^- p} \approx \lambda_{e^+ n} \approx 0.448 T_{\mathrm{MeV}}^5 \, \mathrm{s}^{-1}, \tag{67}$$

where we have neglected the neutron-proton mass difference, and have assumed that the initial state electrons and positrons are extremely relativistic. These approximations are

reasonable at $T \gtrsim 1$ MeV, and become invalid when T approaches 0.5 MeV. However, these reaction rates are negligible compared with those in equations (65a) and (65b) at $T \lesssim 1$ MeV. This is because at these low temperatures, (i) the number density of electron-positron pairs decreases significantly; and (ii) the cross sections decrease rapidly, especially so for electron capture on proton, which has to overcome the neutron-proton mass difference. Therefore, the breaking-down of the above approximations has no serious consequences for setting the final value of Y_e in the ejecta.

5.2. Determination of Y_e

As noted in §2, the electron fraction Y_e in the ejecta is governed by equation (7). We can rewrite this equation as

$$\dot{Y}_e = \lambda_1 - \lambda_2 Y_e, \tag{68}$$

where $\lambda_1 = \lambda_{\nu_e n} + \lambda_{e^+ n}$, $\lambda_2 = \lambda_1 + \lambda_{\bar{\nu}_e p} + \lambda_{e^- p}$, and $\dot{Y}_e = dY_e/dt = v(dY_e/dr)$. Regardless of the particular forms of λ_1 and λ_2, the general solution to the above equation is given by

$$Y_e(t) = \left[Y_e(0) - \frac{\lambda_1(0)}{\lambda_2(0)} \right] I(0,t) + \frac{\lambda_1(t)}{\lambda_2(t)} - \int_0^t I(t',t) \frac{d}{dt'} \left[\frac{\lambda_1(t')}{\lambda_2(t')} \right] dt', \tag{69}$$

where $t = 0$ is taken as the time when the ejecta leave the neutron star surface at radius R, and where

$$I(t',t) = \exp\{ -\int_{t'}^t \lambda_2(t'')dt'' \} \tag{70}$$

is a "memory" function of the interaction history, with $\int_{t'}^t \lambda_2(t'')dt''$ the total number of interactions on a pair of neutron and proton between t' and t (Qian 1993).

It is easy to show that the first term on the right-hand side of equation (69) quickly vanishes at $t > 0$. The gravitational binding energy of a nucleon at the neutron star surface is $\sim GMm_N/R \sim 200$ MeV. A nucleon has to obtain at least this amount of energy from

the neutrino fluxes in order to escape to large radii. The main heating reactions, ν_e and $\bar{\nu}_e$ absorption on free nucleons, are also responsible for determining Y_e.

From each interaction with the ν_e or $\bar{\nu}_e$ flux, an amount of energy ~ 10–20 MeV per nucleon is absorbed. Therefore, a nucleon in the ejecta has to have at least 10 interactions above the neutron star surface, and the total number of interactions on a pair of neutron and proton in the ejecta satisfies

$$\int_0^\infty \lambda_2(t)dt > \int_0^\infty [\lambda_{\nu_e n}(t) + \lambda_{\bar{\nu}_e p}(t)]dt > 20, \tag{71}$$

where $t = \infty$ is a symbolic time when λ_2 becomes negligibly small.

From the discussions in §3.3, we know that most of the heating interactions take place at temperatures around $T_{\text{eff}} \sim 2$ MeV. So for $T \lesssim 2$ MeV, we can safely assume $I(0, t) \ll 1$ and neglect the first term on the right-hand side of equation (69).

Making use of the relation

$$\frac{d}{dt'}I(t', t) = \lambda_2(t')I(t', t), \tag{72}$$

we can perform integration by parts in the third term on the right-hand side of equation (69), and obtain

$$Y_e(t) \approx \frac{\lambda_1(t)}{\lambda_2(t)} - \frac{1}{\lambda_2(t)}\frac{d}{dt}\left[\frac{\lambda_1(t)}{\lambda_2(t)}\right] \tag{73}$$

when $I(0, t) \ll 1$. In deriving the above equation, we have assumed

$$\frac{1}{\lambda_2(t)}\left|\frac{d}{dt}\left[\frac{\lambda_1(t)}{\lambda_2(t)}\right]\right| \ll \frac{\lambda_1(t)}{\lambda_2(t)}, \tag{74}$$

and therefore, have neglected terms of higher orders in $\lambda_2^{-1}(t)$, i.e., the remaining integral

$$\int_0^t I(t', t)\frac{d}{dt'}\left\{\frac{1}{\lambda_2(t')}\frac{d}{dt'}\left[\frac{\lambda_1(t')}{\lambda_2(t')}\right]\right\} dt'.$$

The condition in equation (74) is called the quasi-equilibrium (QSE) condition. This is because under this condition,

$$Y_e(t) \approx Y_{e,\text{EQ}}(t) - \frac{1}{\lambda_2(t)} \frac{d}{dt} Y_{e,\text{EQ}}(t) \approx Y_{e,\text{EQ}}(t), \tag{75}$$

where

$$Y_{e,\text{EQ}} \equiv \frac{\lambda_1(t)}{\lambda_2(t)} \tag{76}$$

is the instantaneous equilibrium value at time t. From the rates and discussions in §5.1, we see that for $T \lesssim 1$ MeV, λ_1 and λ_2 are dominated by the rate(s) for neutrino absorption on free nucleons. Consequently, $d(\lambda_1/\lambda_2)/dt \approx 0$, and Y_e assumes a constant equilibrium value

$$Y_{e,f} \approx \frac{\lambda_{\nu_e n}}{\lambda_{\nu_e n} + \lambda_{\bar{\nu}_e p}} \approx \left(1 + \frac{L_{\bar{\nu}_e}}{L_{\nu_e}} \frac{\epsilon_{\bar{\nu}_e} - 2\Delta + 1.2\Delta^2/\epsilon_{\bar{\nu}_e}}{\epsilon_{\nu_e} + 2\Delta + 1.2\Delta^2/\epsilon_{\nu_e}} \right)^{-1} \tag{77}$$

for $T \lesssim 1$ MeV (Qian et al. 1993).

The $Y_{e,f}$ given by equation (77) would be the final value of Y_e in the ejecta if equations (7) and (68) were valid for all temperatures. However, as we have discussed before, free nucleons begin to be bound into α-particles and heavier nuclei at $T < 1$ MeV (cf. eq. [62]). Therefore, equations (7) and (68) are to be replaced by

$$\dot{Y}_e = \lambda_1' - \lambda_2' Y_e \tag{78}$$

at $T < 1$ MeV, where $\lambda_1' = \lambda_{\nu_e n} + (\lambda_{\bar{\nu}_e p} - \lambda_{\nu_e n})(1 - X_N)/2$ and $\lambda_2' = \lambda_{\nu_e n} + \lambda_{\bar{\nu}_e p}$. In deriving equation (78), we have neglected the rates for neutrino absorption on α-particles and heavier nuclei and all the electron capture rates, compared with the neutrino absorption rates on free nucleons. We have also assumed $Y_e \approx X_p + (1 - X_N)/2$, where $X_N = X_p + X_n$ is the mass fraction of free nucleons, with X_p and X_n the mass fractions of protons and neutrons, respectively. This approximation for Y_e is good for material mainly composed of free nucleons and α-particles.

Equation (78) is mathematically identical to equation (68). At the transition from equation (68) to (78), we have $Y_e \approx \lambda_1/\lambda_2 \approx \lambda'_1/\lambda'_2$ and $d(\lambda_1/\lambda_2)/dt \approx d(\lambda'_1/\lambda'_2)/dt \approx 0$. From the general solution given in equation (69), we can easily show that

$$Y_e(t) \approx \frac{\lambda'_1(t)}{\lambda'_2(t)}, \tag{79}$$

provided the QSE condition

$$\frac{1}{\lambda'_2(t)} \left| \frac{d}{dt} \left[\frac{\lambda'_1(t)}{\lambda'_2(t)} \right] \right| \ll \frac{\lambda'_1(t)}{\lambda'_2(t)} \tag{80}$$

is satisfied. From the expression for λ'_1, we see that the QSE condition in equation (80) depends on how fast X_N is changing. In turn, the rate at which X_N changes is determined by the thermodynamic and hydrodynamic conditions in the ejecta (cf. eq. [62]).

Typically, the QSE condition in equation (80) is no longer met when

$$\lambda'_2(r) \frac{r}{v(r)} \sim 1. \tag{81}$$

At this point, the neutrino absorption reactions are not frequent enough to change Y_e any more, and Y_e "freezes" out at the last achievable instantaneous equilibrium value

$$Y'_{e,f} \approx \frac{\lambda_{\nu_e n}}{\lambda_{\nu_e n} + \lambda_{\bar{\nu}_e p}} + \frac{1 - X_N}{2} \frac{\lambda_{\bar{\nu}_e p} - \lambda_{\nu_e n}}{\lambda_{\nu_e n} + \lambda_{\bar{\nu}_e p}}. \tag{82}$$

Therefore, if the QSE condition for equation (78) is still satisfied when a significant fraction of the material is in α-particles and heavier nuclei, the final Y_e in the ejecta will deviate from $Y_{e,f}$ given in equation (77). The influence of α-particles and heavier nuclei on Y_e in the ejecta was first pointed out by Fuller & Meyer (1995).

Because the evolution of Y_e in the ejecta at $T < 1$ MeV is coupled with the change in the nuclear composition of the ejecta, and depends sensitively on the thermodynamic and hydrodynamic conditions in the ejecta (cf. eqs. [62] and [81]), we will follow Y_e numerically in the nucleosynthesis calculations to be presented in a separate paper (Hoffman et al.

1996b). However, whether the final Y_e in the ejecta is given by equation (77) or (82), mathematically, $Y_e = 0.5$ corresponds to

$$\lambda_{\bar{\nu}_e p} \approx \lambda_{\nu_e n}, \tag{83}$$

barring the unlikely case where the QSE condition for equation (78) holds until all the free nucleons disappear. The qualitative feature of heavy element nucleosynthesis depends crucially on whether $Y_e > 0.5$ or $Y_e < 0.5$. From equations (65a), (65b), and (83), we see that neutrino luminosities and energy distributions have direct bearings on the nature of heavy element nucleosynthesis in supernovae.

5.3. Neutrino two-color plot

As the neutrinos diffuse towards the edge of the neutron star, their interactions with matter decrease with the decreasing temperature and density. Gradually, they decouple from the thermodynamic equilibrium with the neutron star matter, keeping energy distributions corresponding to the conditions (e.g., temperature, density, chemical composition) in the decoupling region. Because only energy-exchange processes are directly responsible for achieving thermodynamic equilibrium, and different neutrino species have different ability to exchange energy with matter, the thermodynamic decoupling processes of different neutrino species occur in different regions of the neutron star. In turn, each neutrino species emerges from the neutron star with its own characteristic energy distribution.

All neutrino species exchange energy with electrons. In fact, the neutral-current scattering on electrons is the main energy-exchange process for ν_μ, $\bar{\nu}_\mu$, ν_τ, and $\bar{\nu}_\tau$. On the other hand, although ν_e and $\bar{\nu}_e$ have the extra charged-current scattering on electrons which ν_μ, $\bar{\nu}_\mu$, ν_τ, and $\bar{\nu}_\tau$ lack, they exchange energy with matter even more efficiently through

the charged-current absorption reactions on nucleons given in equations (8a) and (8b). Therefore, ν_μ, $\bar{\nu}_\mu$, ν_τ, and $\bar{\nu}_\tau$ decouple at higher temperature and density inside the neutron star than ν_e and $\bar{\nu}_e$, and correspondingly, their energy distributions are harder than those of ν_e and $\bar{\nu}_e$.

As we have seen in §5.2, the luminosities and energy distributions for ν_e and $\bar{\nu}_e$ have significant effects on Y_e, or equivalently, the neutron excess in the wind. In addition, emission of ν_e and $\bar{\nu}_e$ is coupled with the deleptonization process of the neutron star, which makes the problem of ν_e and $\bar{\nu}_e$ transport in the neutron star even more complicated. In what follows, we give a more detailed discussion of the time evolution of ν_e and $\bar{\nu}_e$ emission in supernovae.

Shortly after the creation of the neutron star by the core collapse and subsequent supernova explosion, its neutron concentration is larger than, but still comparable to its proton concentration. Because ν_e and $\bar{\nu}_e$ exchange energy with matter mainly through absorption on neutrons and protons, respectively, ν_e can stay in thermodynamic equilibrium with the neutron star matter down to somewhat lower temperatures and densities than $\bar{\nu}_e$. In other words, $\bar{\nu}_e$ decouple at slightly higher temperatures than ν_e, and have a slightly larger average energy, i.e., $\langle E_{\bar{\nu}_e} \rangle \gtrsim \langle E_{\nu_e} \rangle$. The luminosities for ν_e and $\bar{\nu}_e$ are about the same, so the number flux of ν_e is larger than that of $\bar{\nu}_e$. This results in a net electron lepton number flux leaking out of the neutron star, which reflects the net deleptonization process of converting protons into neutrons through electron capture inside the neutron star. Meanwhile, the neutron star is shrinking to its final equilibrium configuration. The heating caused by the compression raises the temperature of the neutron star interior. As a result, both $\langle E_{\bar{\nu}_e} \rangle$ and $\langle E_{\nu_e} \rangle$ increase initially while keeping $\langle E_{\bar{\nu}_e} \rangle \gtrsim \langle E_{\nu_e} \rangle$.

Because of the diffusive nature of the neutrino transport processes, we expect to see the strongest deleptonization in the surface layers of the neutron star. As these surface layers

become more and more neutron rich due to the deleptonization, the decoupling regions for ν_e and $\bar{\nu}_e$ are progressively separated from each other. The deleptonization effects on $\langle E_{\nu_e} \rangle$ and $\langle E_{\bar{\nu}_e} \rangle$ are most pronounced when the neutron star approximately reaches its final radius and the compressional heating becomes negligible. At this point, $\langle E_{\bar{\nu}_e} \rangle$ still increases because $\bar{\nu}_e$ decouple deeper with the deleptonization. On the contrary, $\langle E_{\nu_e} \rangle$ begins to decrease as ν_e decouple further out in the neutron star due to the increasing neutron concentration in the surface layers.

Schematically, we can illustrate the time evolution of the ν_e and $\bar{\nu}_e$ energy distributions on a two-dimensional plot. We choose the abscissa and ordinate to be ϵ_{ν_e} and $\epsilon_{\bar{\nu}_e}$, respectively, because these energies are more directly related to our discussion of Y_e in the ejecta (cf. eqs. [65a] and [65b]). Borrowing a term from optical photometry, we refer to this plot as the "neutrino two-color plot." For a particular supernova model, the time evolution of ϵ_{ν_e} and $\epsilon_{\bar{\nu}_e}$ is represented by a contour line on this plot. Taking ϵ_{ν_e} and $\epsilon_{\bar{\nu}_e}$ as functions of time from Fig. 3 in Woosley et al. (1994), we present an example plot in Fig. 5. The solid contour line in Fig. 5 shows the evolution track of ϵ_{ν_e} and $\epsilon_{\bar{\nu}_e}$. The open circles on this track indicate the time after the onset of the collapse in intervals of approximately $1/3$ s for $t \approx 0$–4 s and approximately 1 s for $t \approx 4$–18 s. Time $t \approx 0$ corresponds to the open circle at the lower left corner of the plot, and time increases thereafter along the track to $t \approx 18$ s at the last open circle. The evolution of ϵ_{ν_e} and $\epsilon_{\bar{\nu}_e}$ slows down considerably at $t > 10$ s. As a result, there are two overlapping open circles at $t \approx 12$, 14, and 17 s (i.e., the open circles for $t \approx 13$, 15, and 18 s cannot be distinguished). From this plot, we can see that ϵ_{ν_e} and $\epsilon_{\bar{\nu}_e}$ both increase for $t \approx 0$–1 s, and ϵ_{ν_e} starts to decrease while $\epsilon_{\bar{\nu}_e}$ increases for $t \gtrsim 2$ s, in agreement with our previous discussion. The evolution of ϵ_{ν_e} and $\epsilon_{\bar{\nu}_e}$ during $t \approx 1$–2 s is more complicated and may only be understood by more involved argument than our previous qualitative discussion.

Numerical supernova calculations show that shortly after the explosion, the ratio $L_{\bar{\nu}_e}/L_{\nu_e}$ always stays close to 1 (see, e.g., Fig. 2 in Woosley et al. 1994). Therefore, without specific detailed neutrino transport calculations, we can divide the neutrino two-color plot into three regions corresponding to $Y_e < 0.5$, $Y_e \approx 0.5$, and $Y_e > 0.5$ in the ejecta. The region corresponding to $Y_e \approx 0.5$ is bounded by the range of values for $L_{\bar{\nu}_e}/L_{\nu_e}$, and is determined by equation (83). In Fig. 5, we give an example situation where this region is bounded by $L_{\bar{\nu}_e}/L_{\nu_e} \approx 1.1$ from below and by $L_{\bar{\nu}_e}/L_{\nu_e} \approx 1.0$ from above. The parameter space to the left of this region corresponds to $Y_e < 0.5$, and the parameter space for $Y_e > 0.5$ lies to the right of this region. In general, our neutrino two-color plot can be presented similarly for any supernova model. The implications of this plot for heavy element nucleosynthesis in supernovae are discussed in the next subsection.

5.4.   Nucleosynthesis implications of the neutrino two-color plot

As discussed in §1, a severe failure of r-process calculations in the neutrino-driven wind is the overproduction of nuclei in the vicinity of $N = 50$ at $t \sim 1$ s after the supernova explosion. Hoffman et al. (1996a) have shown that this failure can be turned into an attractive feature if Y_e in the ejecta is slightly increased from the value in Wilson's supernova model to $0.484 \lesssim Y_e \lesssim 0.488$, for which some light p-process nuclei can be produced. From Fig. 5, we see that the evolution trajectory of $\epsilon_{\bar{\nu}_e}$ and ϵ_{ν_e} for $t \sim 1$ s lies entirely in the region of $Y_e \approx 0.5$ on the neutrino two-color plot. This implies that some small uncertainties in the supernova model predictions for $\epsilon_{\bar{\nu}_e}$, ϵ_{ν_e}, and/or $L_{\bar{\nu}_e}$, L_{ν_e} may explain the overproduction of the nuclei in the vicinity of $N = 50$. It also hints that future supernova models with more accurate neutrino transport calculations may not encounter the overproduction problem, but would facilitate the nucleosynthesis of some light p-process nuclei instead.

On the other hand, we see that $\epsilon_{\bar{\nu}_e}$ and ϵ_{ν_e} predicted by Wilson's supernova model will clearly give $Y_e < 0.5$ in the neutrino-heated ejecta for $t > 3$ s. For any r-process nucleosynthesis to take place in the ejecta, we must have $Y_e < 0.5$. Therefore, the neutrino two-color plot in Fig. 5 at least signifies the possibility of an r-process for $t > 3$ s in Wilson's supernova model, even in the presence of some small uncertainties in the predicted neutrino characteristics. While the exact values of Y_e in the ejecta depend on the accuracy of supernova neutrino transport calculations on the one hand, and the thermodynamic and hydrodynamic conditions in the ejecta on the other hand, we feel that the neutrino two-color plot has some interesting implications for the nature of supernova nucleosynthesis. Perhaps the nucleosynthesis of some light p-process nuclei can occur at $t \sim 1$ s, and the r-process nucleosynthesis is produced later when the neutrino characteristics evolve to the neutron-rich region of the neutrino two-color plot.

6.   Conclusions and Discussion

The principal conclusions of our paper are simple analytic expressions, verified by comparison to numerical simulation, for the entropy (eqs. [48a] and [48b]), mass loss rate (eqs. [58a] and [58b]), and dynamic time scale (eq. [61]) in the neutrino-driven wind. We have also given a detailed analysis of how Y_e is determined (§5) in the wind.

We began this work in the hope that a simple physical model would yield the conditions required by Woosley et al. (1994) for the r-process, in particular rapid expansion time scales and entropies of order 300 or more. While pursuing this quest, a great deal was learned about the properties of neutrino-driven winds, which eventually came to appear quite simple. Mutually confirming analytic and numerical calculations give the solutions in Table 1. These models span a range of gravitational potential and neutrino luminosity that

should typify the Kelvin-Helmholtz evolution of most neutron stars.

Unfortunately, none of the models in Table 1 will give a good r-process unless Y_e is very low (Hoffman et al. 1996b). Nor can one continually increase the entropy by turning the neutrino luminosity down. The entropy only increases as the sixth root of L_ν while the mass loss rate declines as $L_\nu^{5/3}$ (assuming that the neutrino energy distributions stay more or less the same over the period of interest, cf. Fig. 5). Moreover, the dynamic time scale becomes unacceptably long. We conclude that one of the following must be true: (1) the (heavy) r-process isotopes are not made in the neutrino-powered wind of young neutron stars (of the type given in Table 1); (2) the nuclear physics of the r-process is at fault (presently unlikely); or (3) important physics has been left out of the models in Table 1. We shall spend the remainder of the paper discussing the third possibility.

What has been left out? First, there are effects that we know exist and can estimate — general relativity and nucleon recombination. In §4.2 we provided numerical calculations in a post-Newtonian approximation to show the effects of general relativity. Any effect that strengthens the gravitational potential leads to higher entropy in the wind (§3.3.1). The essential consequences of general relativity on our models can be obtained simply by increasing the effective mass of the neutron star — e.g., Models 10DEF vs. Models 10ABC. We also considered, however, in a post-Newtonian calculation, the extreme case of a neutron star having a radius of 10 km and a gravitational mass (at infinity) of 2 $M_\odot$. This was the only calculation without an artificial energy source that gave an entropy over 200. Perhaps the heavy r-process is made in neutron stars that are on their way to becoming black holes. However, one cannot extend this approach indefinitely. At some point, not much beyond the extreme case considered, as the gravitational potential deepens, the neutron star becomes unstable for any equation of state and turns into a black hole on a dynamic (collapse) time scale. Whether sufficient matter is ejected from such objects to make the

solar r-process abundances remains to be determined.

The recombination of nucleons into α-particles releases an amount of energy of about $\Delta Q \sim 7$ MeV per nucleon. Assuming most of the nucleons recombine at $T \sim 0.5$ MeV, we get an additional entropy of about $\Delta S \sim \Delta Q/T \sim 14$. This was not included in either the numerical or analytic models and should be added to all the entropies calculated in the paper.

Our treatment of neutrino-antineutrino annihilation is very approximate (cf. Janka 1991a,b) and there are expectations that a more realistic treatment might lead to a moderate increase in the entropy (§4.5) and reduction in the dynamic time scale. Our opinion is that this is too small a change to restore the r-process.

It is rather unfortunate that we did not get or understand the high entropies obtained in Wilson's supernova model used by Woosley et al. (1994) for the r-process calculations. We note that Wilson's supernova model derives from a fully general relativistic hydrodynamic code with a consistent and detailed treatment of neutrino transport. However, the origin of the discrepancies in entropy between our study and Wilson's numerical calculations remains unknown and is still under investigation.

In §4.6 we considered the effect of a time variable luminosity and found that, while the entropy did not change much, considerable leverage could be exercised on the expansion time scale. Perhaps the r-process is made in those regions of the wind that begin their ejection at low neutrino luminosity, but absorb additional energy and expand faster as the local neutrino luminosity increases.

Indeed, the dynamic time scale is an important third parameter not sufficiently emphasized in previous studies of the r-process in the wind. For a given Y_e, increasing the neutron-to-seed ratio can be achieved either by reducing the reaction rates that assemble

α-particles into heavy nuclei, i.e., by reducing the density (raising the entropy) or by decreasing the time during which these reactions can operate. Since the rate of α-burning goes approximately as ρ^3 (Woosley & Hoffman 1992), one can obtain approximately the same r-process at one-half the requisite entropy if the time scale is about 8 times shorter. One general result of our study is that it is easier to achieve a more vigorous outflow than it is to increase the entropy, thus to some extent the quest for $S \gtrsim 300$ may be misguided. Entropies of ~ 150, which are readily achievable may function equally well if the expansion time scale can be cut by an order of magnitude to ~ 0.01 s.

The most effective way of accelerating the expansion, and, as it turns out, of increasing the entropy, is to provide an additional source of energy of order 10^{48} erg s^{-1} at between 1.5 and 3 times the neutron star radius. This is a region where the mass loss rate has, for the most part, already been determined, but the freeze-out of α-particles from NSE ($T \approx 5 \times 10^9$ K) has not yet occurred. The effect of a purely arbitrary energy source was explored in §4.4. The origin of such energies brings us to effects that might be there, but which are very difficult to estimate.

First, we know that fall-back will occur as the supernova explosion develops. Convection becomes less important to the explosion mechanism as time passes, but material is still decelerated to below the escape speed as the shock interacts with the stellar mantle. Woosley & Weaver (1995) find that typically ~ 0.1 $M_\odot$ falls back in about 10^4 s (more earlier than later), so one expects this accreted material to be adding mass faster than the wind is removing it. However, the hydrodynamic interaction is complex. It is uncertain whether *any* material finds its way back to the neutron star during the first 20 s of interest. But the entropy of the infalling material is much lower and it may descend in plumes while the wind rises in large bubbles. It may even be that the wind is derived from the accreted material rather than the neutron star itself. It is difficult to guess what the actual

interaction will be of the plumes with the neutron star, but it may be that the wind starts with an initial entropy higher (from the accretion shock) than the steady-state value derived here. Electron capture near the neutron star would also influence the starting value of Y_e.

A ten-second-old neutron star will also be the site of continuing energetic activity other than its neutrino emission. In particular, the star may be violently vibrating, rotating rapidly, or have a strong magnetic field. Small oscillations at the base of the developing neutron star crust will steepen into shocks in the steep density gradient at the neutron star surface (Woosley 1996). This must certainly occur at some level, but whether it leads to $\sim 10^{48}$ erg s^{-1} being deposited at greater than 1.5 neutron star radii for a ten-second-old neutron star is unclear.

The magnetic field configuration near the surface of a newly born neutron star is very uncertain — both its spatial structure and strength — but there are speculations (Duncan & Thompson 1992) that the magnetic field may be very large, $\sim 10^{15}$ gauss. Since the outer layers of the neutron star have recently been convective, the field structure near the surface may be highly tangled. A 10^{15} gauss field could confine, or at least impede the escape of plasma having a temperature of 4 MeV, i.e., greater than the neutrinosphere temperature at late times. Such a field could have several effects. To the extent that it impedes the outflow of the wind, its effect resembles that of a stronger gravitational potential. Higher entropy is a likely outcome. To the extent the field reconnects at higher altitudes, because of rotational shearing or stretching in the wind, it provides the desired extra heating. Flow in the field may also develop clumps, the analogue of "photon bubbles" studied in x-ray pulsars (Klein & Arons 1989, 1991).

If the dynamic time scale and entropy are inadequate, one may have to turn to a significant lowering of Y_e. As discussed in §5, Y_e in the ejecta is determined by neutrino emission characteristics of the neutron star. In turn, the neutrino luminosity and energy

spectrum are determined by neutrino interactions in the hot dense neutron star (§5.3). Any uncertainty in our understanding of neutrino interactions in hot dense matter causes an inaccurate prediction of the emission properties. For example, some recent studies (Keil, Janka, & Raffelt 1995; Sawyer 1995) suggest that the strength of neutrino interactions is reduced by the medium response of nuclear matter, with respect to the case of neutrino interactions with a single nucleon. Although it is not clear whether the effects found by these studies on neutrino characteristics can change Y_e in the ejecta significantly, a complete picture of supernova nucleosynthesis may await better knowledge of neutrino interactions in hot dense matter.

Finally, the neutrino characteristics above the neutron star surface can be altered by the process of neutrino flavor transformation. For example, if ν_μ or ν_τ has a cosmologically significant mass in the range of 1–100 eV and the mass of ν_e is much smaller, then ν_μ or ν_τ will be transformed into ν_e above the neutron star surface through the Mikheyev-Smirnov-Wolfenstein (MSW) mechanism (Fuller et al. 1992; Qian et al. 1993). Because ν_μ and ν_τ have a higher average energy than $\bar{\nu}_e$, conversion of ν_μ or ν_τ into ν_e will increase Y_e in the ejecta (cf. eq. [77]). Such flavor transformation is undesirable (Qian et al. 1993). On the other hand, if ν_e has a mass of a few eV and ν_μ or ν_τ is much lighter, then $\bar{\nu}_\mu$ or $\bar{\nu}_\tau$ will be transformed into $\bar{\nu}_e$ above the neutron star surface (Qian 1993; Qian & Fuller 1995). In this case, conversion of $\bar{\nu}_\mu$ or $\bar{\nu}_\tau$ into $\bar{\nu}_e$ can significantly reduce Y_e in the ejecta (Fuller, Qian, & Wilson 1996). In view of the recent claim of possible evidence for $\bar{\nu}_\mu \rightarrow \bar{\nu}_e$ oscillations by the LSND experiment (Athanassopoulos et al. 1995) and other astrophysical evidence for massive neutrinos (see, e.g., Fuller, Primack, & Qian 1995), this latter process of flavor transformation is worth further exploring.

REFERENCES

Athanassopoulos, C. et al. 1995, Phys.Rev.Lett, 75, 2650

Bethe, H. A. 1993, ApJ, 412, 192

Burrows, A. & Mazurek, T. J. 1982, ApJ, 259, 330

Duncan, R. C., Shapiro, S. L., & Wasserman, I. 1986, ApJ, 309, 141

Duncan, R. C. & Thompson, C. 1992, ApJ, 392, L9

Fuller, G. M., Mayle, R., Meyer, B. S., & Wilson, J. R. 1992, ApJ, 389, 517

Fuller, G. M. & Meyer, B. S. 1995, ApJ, 453, 792

Fuller, G. M., Primack, J. R., & Qian, Y.-Z. 1995, Phys.Rev.D, 52, 1288

Fuller, G. M., Qian, Y.-Z., & Wilson, J. R. 1996, in preparation

Fuller, G. M., Woosley, S. E., & Weaver, T. A. 1986, ApJ, 307, 675

Hoffman, R. D., Woosley, S. E., Fuller, G. M., & Meyer, B. S. 1996a, ApJ, 460, 478

Hoffman, R. D., Woosley, S. E., Qian, Y.-Z., & Fuller, G. M. 1996b, in preparation

Howard, W. M., Goriely, S., Rayet, M., & Arnould, M. 1993, ApJ, 417, 713

Janka, H.-Th. 1991a, Ph.D. thesis, MPA-Report 587

Janka, H.-Th. 1991b, A&A, 244, 378

Janka, H.-Th. 1995, Astroparticle Physics, 3, 377

Janka, H.-Th. & Müller, E. 1995, ApJ, 448, L109

Keil, W., Janka, H.-Th., & Raffelt, G. 1995, Phys.Rev.D, 51, 6635

Klein, R. I. & Arons, J. 1989, in Proc. of the 23rd ESLAB Symposium in X-Ray Astronomy, Vol. 1, EAS SP-296, ed. N. White & T. Guyenne (Paris: European Space Agency), 89

Klein, R. I. & Arons, J. 1991, in Stellar Atmospheres: Beyond Classical Models, ed. L. Crivillari (Boston: Kluwer), 205

Meyer, B. S. 1995, ApJ, 449, L55

Meyer, B. S., Howard, W. M., Mathews, G. J., Woosley, S. E., & Hoffman, R. D. 1992, ApJ, 399, 656

Munakata, H., Kohyama, Y., & Itoh, N. 1985, ApJ, 296, 197, see also (errata) ApJ, 304, 580

Qian, Y.-Z. 1993, Ph.D. thesis, University of California, San Diego

Qian, Y.-Z., Fuller, G. M., Mathews, G. J., Mayle, R. W., Wilson, J. R., & Woosley, S. E. 1993, Phys.Rev.Lett, 71, 1965

Qian, Y.-Z. & Fuller, G. M. 1995, Phys.Rev.D, 52, 656

Sawyer, R. F. 1995, Phys.Rev.Lett, 75, 2260

Shapiro, S. L., & Teukolsky, S. A. 1983, *Black Holes, White Dwarfs and Neutron Stars*, (Wiley & Sons: New York), p. 125

Takahashi, K., Witti, J., & Janka, H.-Th. 1994, A&A, 286, 857

Timmes, F. X., Woosley, S. E. & Weaver, T. A. 1996, ApJ, 457, 834

Tubbs, D. L. & Schramm, D. N. 1975, ApJ, 201, 467

Weaver, T. A., Zimmerman, G. B., & Woosley, S. E. 1978, ApJ, 225, 1021

Wilson, J. R. 1996, private communication

Witti, J., Janka, H.-Th., & Takahashi, K. 1994, A&A, 286, 841

Woosley, S. E. 1993, A&AS, 97, 205

Woosley, S. E. 1996, in preparation

Woosley, S. E. & Baron, E. 1992, ApJ, 391, 228

Woosley, S. E. & Hoffman, R. D. 1992, ApJ, 395, 202

Woosley, S. E., Wilson, J. R., Mathews, G. J., Hoffman, R. D., & Meyer, B. S. 1994, ApJ, 433, 229

Figure Captions:

Fig. 1 Conditions in the numerical model for a neutrino-driven wind assuming Newtonian physics, a total neutrino luminosity in all flavors of 6×10^{51} erg s^{-1}, and a neutron star mass and radius of 2.0 $M_\odot$ and 10 km, respectively (Model 10E). The top frame gives the dimensionless entropy per baryon S_{tot} (long dashed line), rate for net energy deposition by neutrinos, $\dot{q}$, in 10^{20} erg g^{-1} s^{-1} (short dashed line), and mass outflow rate, $\dot{M} = 4\pi r^2 \rho v$, in units of 10^{-5} $M_\odot$ s^{-1} (solid line), as functions of radius in km. Note the abrupt decline in $\dot{q}$ at 35 km as the nucleons recombine. The bottom frame gives the density, ρ, in 10^5 g cm^{-3} (solid line), temperature, T, in 10^9 K (long dashed line), and outflow velocity, v, in 10^7 cm s^{-1} (short dashed line), all on the same radial scale.

Fig. 2 Conditions in the numerical model for a neutrino-driven wind from a neutron star of 1.4 $M_\odot$ with a radius of 30 km and a total neutrino luminosity of 6×10^{52} erg s^{-1} (Model 30B). Notation and quantities edited are the same as in Fig. 1, except that the density is in 10^7 g cm^{-3} and the mass outflow rate is in units of 10^{-4} $M_\odot$ s^{-1} for display purposes.
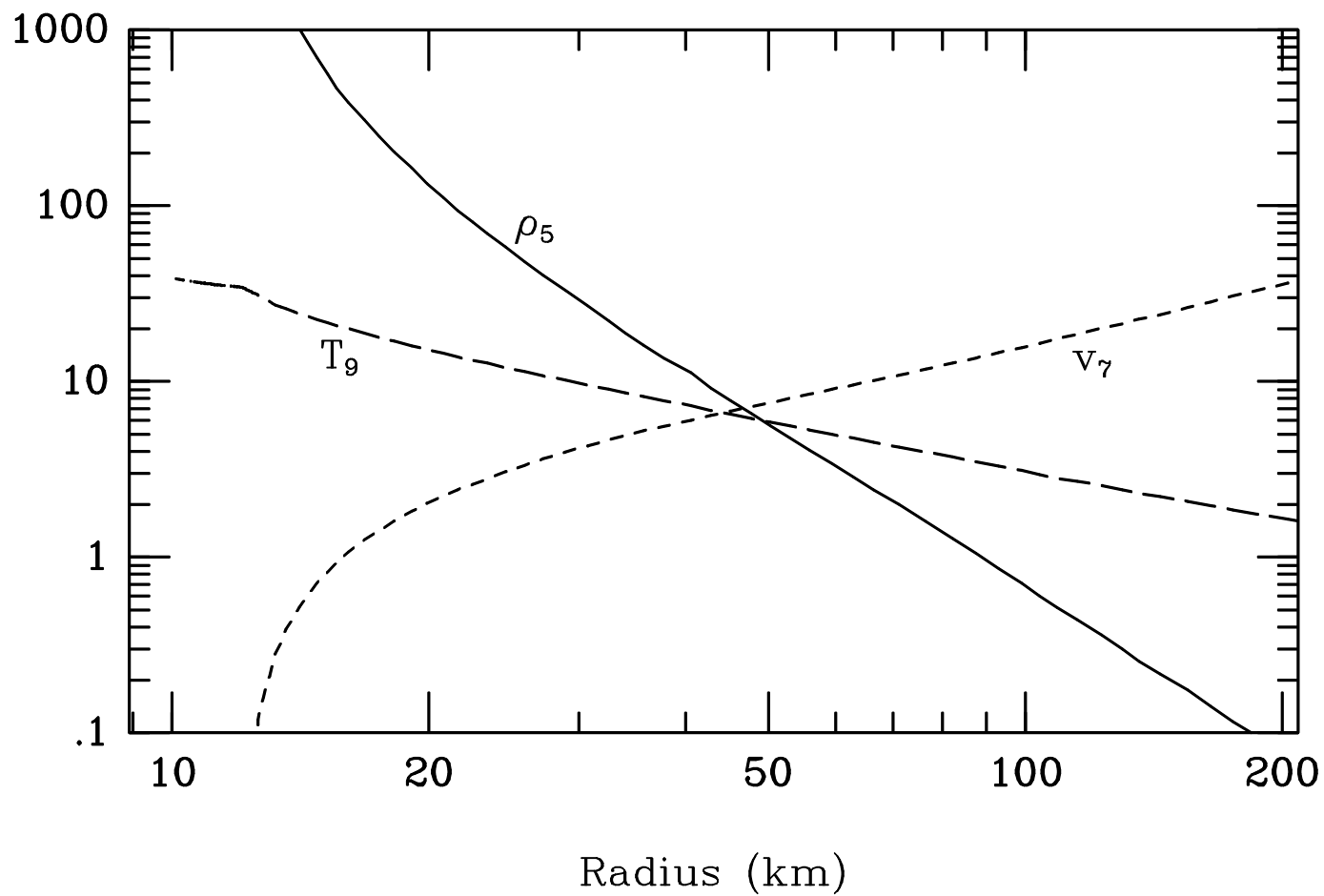
Fig. 3 Effect of a boundary pressure equivalent to a boundary temperature of 2×10^9 K in Model 10E. The total entropy, temperature, and outflow velocity are given as functions of radius. The solid lines are for Model 10E without the boundary pressure, and the corresponding conditions for the same model with the boundary pressure are shown as dashed lines.

Fig. 4 Conditions in the numerical model for a neutrino-driven wind assuming Newtonian physics, a total neutrino luminosity of 3.6×10^{51} erg s^{-1}, and a neutron star mass and radius of 2.0 $M_\odot$ and 10 km, respectively (Model 10F), when an additional (artificial) energy source of 5×10^{47} erg s^{-1} is evenly spread (by volume) between 15 and 25

km (1.5 and 2.5 neutron star radii). Notation and quantities edited are the same as in Fig. 1.

Fig. 5 Neutrino two-color plot. The time evolution of the $\bar{\nu}_e$ and ν_e mean energies, $\epsilon_{\bar{\nu}_e}$ and ϵ_{ν_e}, respectively, predicted by Wilson's supernova model, is shown as a solid contour on the plot. The open circles on this contour indicate the time after the onset of the collapse from $t \approx 0$ at the lower end to $t \approx 18$ s at the upper end. Time increases along the contour in intervals of approximately $1/3$ s for $t \approx 0$–4 s and approximately 1 s for $t \approx 4$–18 s. Note that due to the slow evolution of $\epsilon_{\bar{\nu}_e}$ and ϵ_{ν_e} at $t > 10$ s, there are two overlapping open circles at $t \approx 12$, 14, and 17 s (i.e., the open circles for $t \approx 13$, 15, and 18 s cannot be distinguished). Three regions, separated by the two dashed lines, correspond to values of $\epsilon_{\bar{\nu}_e}$ and ϵ_{ν_e} which would give $Y_e > 0.5$, $Y_e \approx 0.5$, and $Y_e < 0.5$, respectively, in the neutrino-driven wind. See text for detailed explanation.

Top panel labels: S_{tot}, Model 10E, $L_{\nu} = 6 \times 10^{51}$ erg s^{-1}, $\dot{q}\,/10^{20}$ erg g^{-1} s^{-1}, $\dot{M}\,/10^{-5}$ M$_{\odot}$ s^{-1}

Bottom panel labels: ρ_5, T_9, v_7
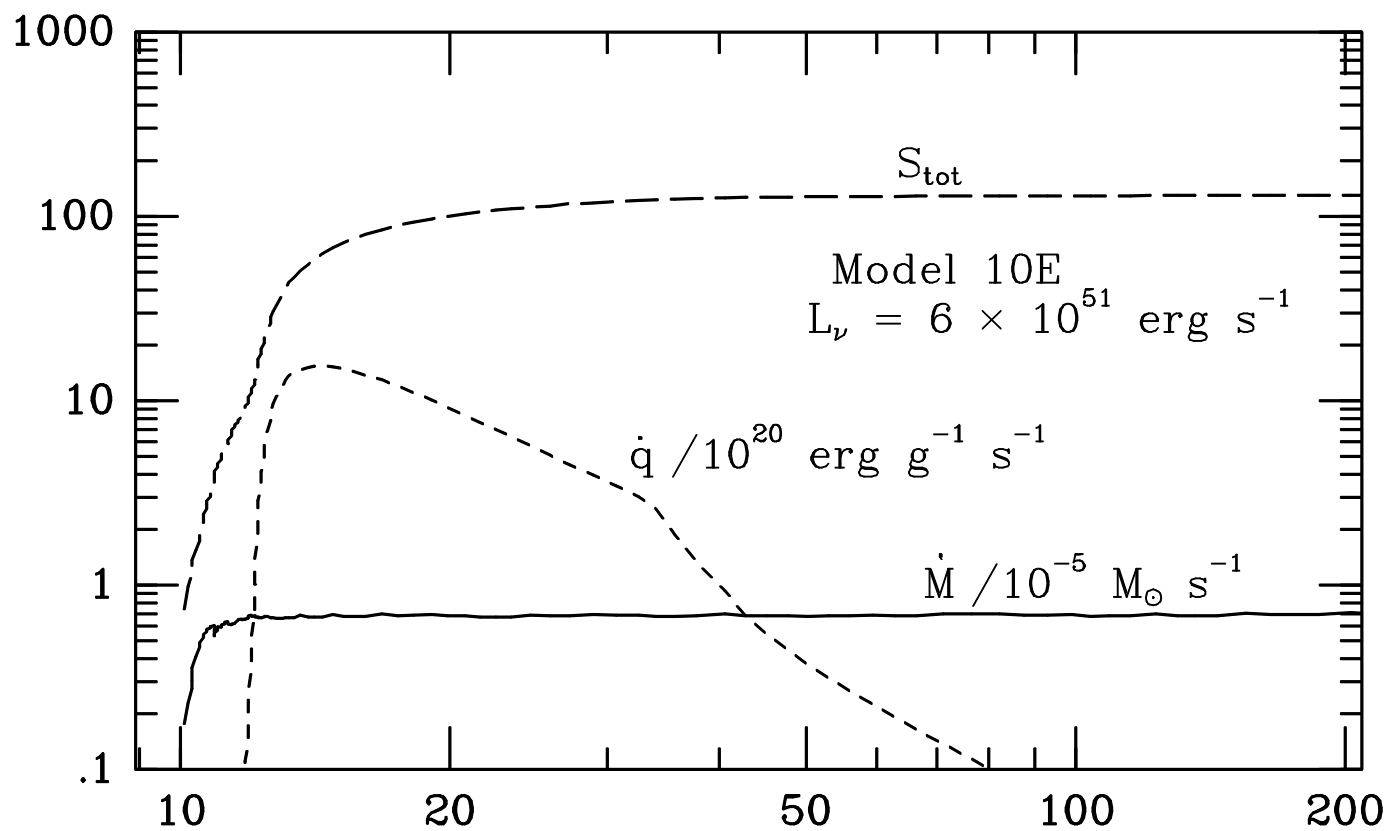
Radius (km)

Table 1: Numerical models and analytic results

Model	Mass $(M_\odot)$	Radius (km)	$L_{\nu\,\text{tot}}$ $(10^{53}$ erg s$^{-1})$	Power (N)[a] (erg s^{-1})	Power (T)[a] (erg s^{-1})
10A	1.4	10	0.18	2.9(49)	2.0(49)
10B	1.4	10	0.06	4.1(48)	3.2(48)
10C	1.4	10	0.036	1.7(48)	1.4(48)
10D	2.0	10	0.18	2.0(49)	1.8(49)
10E	2.0	10	0.06	3.0(48)	2.9(48)
10F	2.0	10	0.036	1.2(48)	1.3(48)
30A	1.4	30	1.8	5.5(51)	6.7(51)
30B	1.4	30	0.6	8.0(50)	1.1(51)
30C	1.4	30	0.36	3.2(50)	4.6(50)

Model	$\dot{M}$ (N)[a] $(M_\odot$ s$^{-1})$	$\dot{M}$ (T)[a] $(M_\odot$ s$^{-1})$	Entropy (N)[a] (k/baryon)	Entropy (T)[a] (k/baryon)	τ_{dyn} (N)[a] (s)	τ_{dyn} (T)[a] (s)
10A	9.7(-5)	5.3(-5)	74	78	2.4(-2)	2.7(-2)
10B	1.4(-5)	8.5(-6)	87	91	6.6(-2)	8.1(-2)
10C	5.6(-6)	3.6(-6)	94	98	1.1(-1)	1.4(-1)
10D	4.6(-5)	3.4(-5)	109	103	2.4(-2)	3.3(-2)
10E	6.7(-6)	5.5(-6)	129	121	6.6(-2)	9.8(-2)
10F	2.8(-6)	2.4(-6)	140	130	1.1(-1)	1.6(-1)
30A	7.6(-2)	5.4(-2)	24	26	3.2(-2)	1.5(-2)
30B	1.1(-2)	8.7(-3)	26	28	7.5(-2)	4.6(-2)
30C	4.2(-3)	3.7(-3)	28	30	1.2(-1)	7.7(-2)

[a] "N" stands for numerically determined; "T" for a result from analytic formulae.

Model 30B
$L_{\nu} = 6 \times 10^{52}$ erg s^{-1}

$\dot{M}/10^{-4}$ M$_{\odot}$ s^{-1}

S_{tot}

$\dot{q}/10^{20}$ erg g^{-1} s^{-1}

T_9

ρ_7

v_7

Radius (km)

Figure showing S_{tot}, T_9, and v_7 as functions of Radius (km) for Model 10E with boundary pressure.

Model 10F
$L_\nu = 3.6 \times 10^{51}$ erg s^{-1}
with an artificial energy source

$\dot{q} / 10^{20}$ erg g^{-1} s^{-1}

S_{tot}

$\dot{M} / 10^{-5}$ M$_\odot$ s^{-1}

ρ_5

T_9

v_7

Radius (km)